PHYSICAL OCEANOGRAPHIC MEASUREMENTS IN THE NORTHEASTERN CHUKCHI SEA: 2013

Prepared for

ConocoPhillips, Inc.
P.O. Box 100360
Anchorage, AK 99510-0360

Shell Exploration & Production Company
3601 C Street, Suite 1000
Anchorage, AK 99503

and

Statoil USA E&P, Inc.
3800 Centerpoint Drive, Suite 920
Anchorage, AK 99502

by

Thomas Weingartner
Seth Danielson
Liz Dobbins
Rachel Potter

Institute of Marine Science
University of Alaska
Fairbanks, AK 99775

July 2014

TABLE OF CONTENTS

LIST OF FIGURES

INTRODUCTION

This report summarizes the hydrographic data collected in August–October 2013 from the northeastern Chukchi Sea in areas potentially subject to and influenced by offshore oil-exploration activities. This work is part of the Chukchi Sea Environmental Studies Program sponsored by ConocoPhillips, Shell Exploration & Production Company, and Statoil USA Exploration & Production, Inc. Prior years' data and interpretations are provided in previous reports and the synthesis of Weingartner et al. (2013a) and will not be repeated here in detail. In addition to summarizing the 2013 hydrography, we also have continued further exploration into the seasonal ("summer") retreat of sea-ice over the Chukchi shelf and have expanded the oceanographic analyses to include data sets from complementary programs. These data sets include satellite-tracked drifters (Weingartner et al., 2014), towed CTD surveys in the northeastern Chukchi Sea, and preliminary results from a simple numerical model that explores the subduction of Bering Sea Water into the pycnocline formed between Meltwater and Winter Water.

As noted previously seasonal changes in Chukchi Sea water properties are established by the annual cycles of sea-ice formation and ablation, air-sea heating/cooling and wind-mixing, and transport of waters from Bering Strait. In the summer and early fall, transport through the Strait is northward on average and includes three major water-masses, which following the nomenclature of Coachman et al. (1975) and Walsh et al. (1989) are: cold, salty, nutrient-rich Anadyr Water; warm, fresh, nutrient-poor Alaskan Coastal Water (ACW); and Bering Shelf Water. The latter has properties intermediate between, but nonetheless distinct from, the Anadyr and Alaskan Coastal water-masses. Coachman et al. (1975) maintain that the Anadyr and Bering Shelf water-masses mix to form Bering Sea Water (BSW) north of the Strait, whereas ACW maintains its properties on the Chukchi shelf. In the summer and fall, Chukchi shelf bottom waters often include near-freezing, saline (dense) Winter Water (WW) that formed in winter by freezing over both the Bering and Chukchi seas. Shallow plumes of cool, dilute, surface Meltwater (MW) that is formed by ice melt also may be present.

The mean circulation over the shelf based on the model of Spall (2007) largely agrees with the inferences drawn from the observations (Figure 1). Although the mean flow is nominally northward over much of the shelf, the bulk of the transport proceeds along three principal pathways, with each pathway associated with a distinct bathymetric feature; Herald Canyon, the Central Channel, and Barrow Canyon. These troughs are separated from one another by shoals: Herald Shoal separates Herald Canyon from the Central Channel, and Hanna Shoal separates the Central Channel and Barrow Canyon.

BSW is transported to the northwestern Chukchi, over the central shelf, and northward through the Central Channel (Figure 1; Weingartner et al., 2005; Woodgate et al., 2005). Weingartner et al. (2005) and Weingartner et al. (2013a) suggest that, south of Hanna Shoal, some central-shelf waters flow eastward toward the coast, in agreement with the circulation models of Winsor and Chapman (2004) and Spall (2007). North of the Central Channel, where there are no long-term current measurements, both models suggest the average flow follows the bathymetry around the western and northern flanks of Hanna Shoal before turning southward along the eastern side of the Shoal, eventually turning eastward and northward before entering Barrow Canyon. However, the models also predict that some of the water along the eastern flank of Hanna Shoal penetrates southwestward along the southern flank of the Shoal before turning eastward towards the coast.

Partial corroboration of this flow path is given by Weingartner et al. (2013a). ACW flows northeastward within the Alaskan Coastal Current toward the head of Barrow Canyon, where it merges with waters flowing eastward from the central shelf to form the canyon outflow. Hence in the summer and fall, the canyon outflow contains a horizontally and vertically structured complex of water-masses (Pickart et al., 2005; Shroyer and Plueddemann, 2012) that include ACW, MW, dense WW, BSW, and mixtures of each.

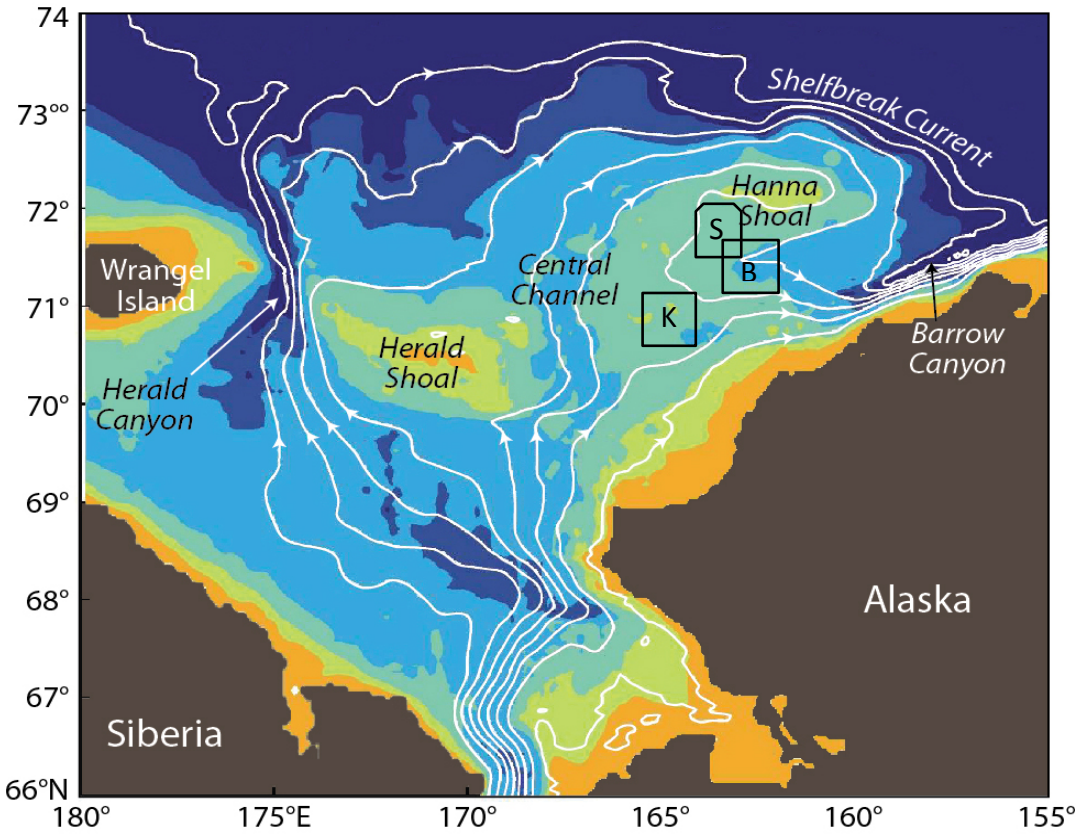

Figure 1. Mean depth-integrated streamlines (white lines) in the Chukchi Sea, after Spall (2007). The bathymetry is color-shaded, and major bathymetric features are labeled. The lettered boxes denote the approximate locations of the Klondike (K), Burger (B), and Statoil (S) study areas.

Two further aspects of the circulation depicted in Figure 1 deserve emphasis. First, for the streamline intersecting the Statoil survey area, the model indicates that the flow is southward through Statoil before veering eastward along the northern edge of the Klondike study area. Weingartner et al. (2013a) suggest that the flow across Statoil is southeastward, at least over the western half of Statoil, with this flow then merging with an eastward flow emanating from Klondike. It appears that these flows converge in the vicinity of the southern half of Burger. Second, the acute curvature of the streamline in Burger implies that water is being carried from the eastern side of Hanna Shoal into Burger before turning back eastward toward the coast. That flow would advect MW in the upper water-column and dense WW in the lower portion of the water-column into and through Burger. Weingartner et al. (2013a) infer that this model prediction is correct, at least intermittently. The implications of these findings are that, in the summer, BSW flows eastward from the Central Channel across both Klondike and the western

half of Statoil. This flow then converges with the waters entering Burger from the northeast. Eventually, all of these water-masses flow eastward and enter Barrow Canyon. The data presented herein suggest that aspects of this circulation prevailed in 2013, although the strong and persistent northeasterly winds in August and September 2013 very likely retarded (or prevented) the northward flow of warm BSW into the northeastern Chukchi Sea.

METHODS

DATA COLLECTION

The sampling discussed in this report was in the northeastern Chukchi Sea and included two cruises, one in August concentrating on the Klondike, Burger and Statoil study areas and, a second in September (through early October) over the same region, but including an extension for the Distributed Biological Observatory (DBO) line into the coast toward Wainwright. The spatial coverage of sampling did not extend over the much broader region surrounding the prospect-specific study areas (Figure 2), as was done in 2011 and 2012. The Klondike study area lies just to the east of the Central Channel, whereas Statoil lies along the southwestern flank of Hanna Shoal and Burger is on the southern flank of this shoal. Water depths in the region are ~40–45 m.

Conductivity, temperature, and depth (pressure) data were collected with a Seabird, Inc., SBE-19+V2 CTD sampling at 4 Hz. This system also included a fluorometer and transmissometer. The instrument was lowered throughout the water column at a rate of ~0.5m min^{-1}, so that ~480 samples were obtained min^{-1}. Measured variables include pressure, temperature, conductivity, beam transmission, and fluorescence. Derived variables include depth, salinity, density, and speed of sound. The data were processed according to the manufacturer's recommended procedures (provided in the SBE Data Processing Manual) and were screened further for anomalous spikes, dropouts, and density inversions. Data were averaged to generate vertical profiles with a resolution of 1 dbar (~1 m). Post-season calibrations of the temperature and conductivity cells were conducted at the manufacturer’s calibration facility. Comparison of the pre- and post-calibration values indicated that the temperature data are accurate to better than 0.005 °C and that the salinity data are accurate to 0.02.

The stations occupied during the two survey cruises are shown in Figure 3, with the color shading indicating the Julian day of the sampling. The 11–23 August survey (Cruise WWW1302) began sampling at Klondike, then moved to the southern half of Burger for a few days until ice prevented further sampling, then sampled ice-free portions of Statoil before returning to the northern half of Burger (much, but not all, of the ice had broken up by then). Ice advance (and retreat) required that the ship move opportunistically back and forth between Burger and Statoil to conduct the sampling. The second survey was conducted between 10 September and 8 October (Cruise WWW1304). This survey commenced in Klondike, then sampled through Burger and Statoil. It then sampled a number of stations between Statoil, Klondike, and Burger, before picking up 5 stations between the southeast corner of Burger and Wainwright. We present these sampling times to emphasize that to some degree the results cannot be considered synoptic given some of the time differences in the sampling. In particular the stations between Klondike and Burger on the second cruise were occupied after the sampling was performed in these two study areas. Consequently, the results presented below may be

temporally aliased because of the lack of synopticity and so data interpretations need to be viewed with respect to this caveat.

We used 3-hourly winds produced by the National Center for Environmental Prediction North American Regional Re-analysis (NARR) model (Mesinger et al., 2006). The NARR wind grid point used in the figures is taken from within Burger (Figure 2) and is representative of conditions over the northeastern Chukchi Sea shelf. Sea ice-concentration maps for selected days from May, June, and July 2013, were prepared to provide a broader perspective of the seasonal evolution in sea ice retreat over the Chukchi shelf prior to the 2013 vessel surveys. The maps were derived from data obtained by the Special Sensor Microwave Imager (SSMI) satellite sensor and processed to Spreen et al. (2008).

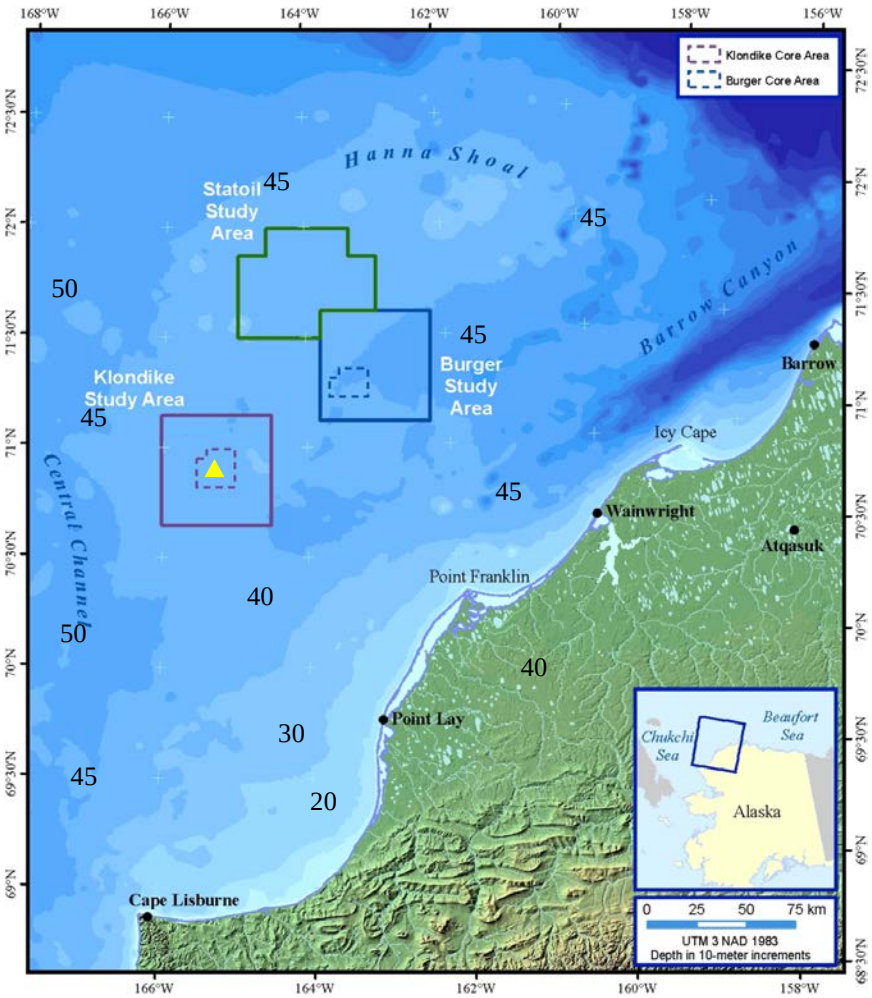

Figure 2. Map showing locations of the Klondike, Burger, and Statoil study areas in relation to the Alaska coast. The yellow triangle shows the approximate location of the NCEP-NARR meteorological grid-point used to assess regional winds.

We also show other sea ice concentration maps of the northeast Chukchi Sea for the period of the surveys. These maps, prepared by G. Premo and J. Andrews of the Shell Ice and Weather Advisory Center, Anchorage, Ak, are based on ice concentration estimates derived from the

high resolution (better than 1 km) data obtained from Radarsat 2, OSCAT, and/or the MODIS satellites.

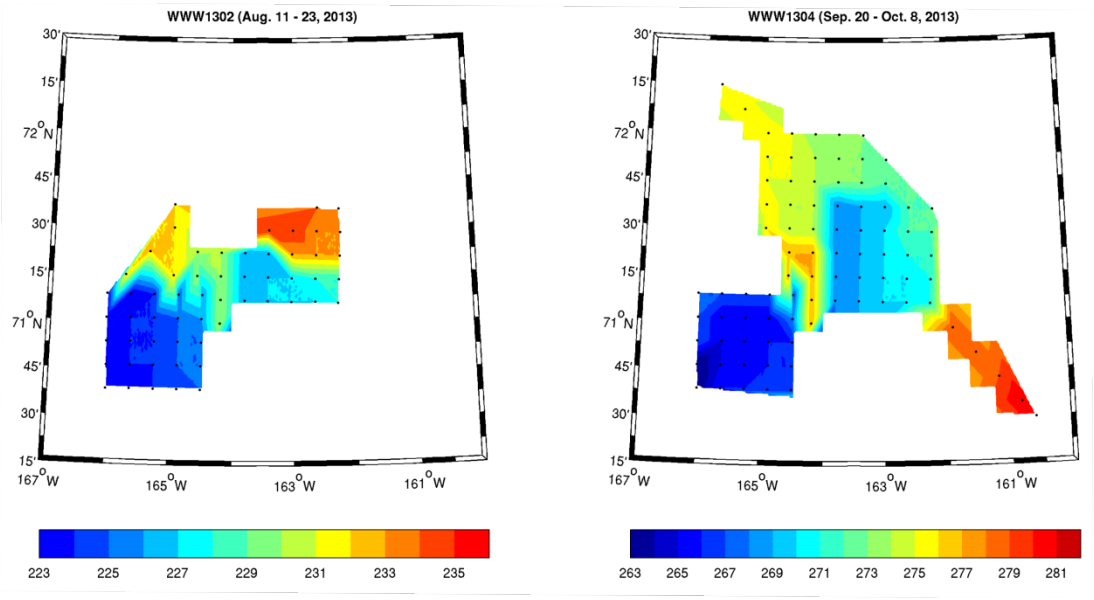

Figure 3. Contour map of the Julian day of the year of CTD station occupations during 2013 sampling, by cruise.

OTHER ANALYSES

We use Empirical Orthogonal Functions (EOF) or Principal Component Analysis (PC) to examine the spatial and temporal variability of May through August sea ice concentrations over the Chukchi Sea shelf for the period of 1979−2013 (the period for which satellite sea ice concentration maps are available). This approach decomposes a spatially and temporally distributed data set into spatial patterns or statistical modes. Each mode has an accompanying time amplitude function, which describes how that spatial pattern varies through time. The intent of a PCA (EOF) analysis is to provide a compact description of the spatial and temporal variability of the data. The modes, derived from the covariance (or correlation) matrix of the original data, have the advantage of being statistically independent of each other. Upon summation (or recombination) the modes (along with their time amplitude function) reproduce the original data set. Hence the procedure is “variance-preserving”. In our analysis of sea ice concentrations we have a large number of variables (ice concentration at each mapped grid point) through time. It is difficult (if not meaningless) to describe the variability at each grid point. Geophysical data, such as Chukchi sea ice concentrations, are often inherently coherent over a variety of spatial and temporal scales. (This contrasts with a purely random data set distributed spatially and temporally.) The purpose of EOFs is to identify (statistically) an ordered set of coherent spatio-temporal patterns so that most of the variability in the original data set can be explained (recovered) by a few modes. The EOF procedure effectively reduces the number of variables (the time series of ice concentration at each gridpoint) into a smaller number of “modes” that more easily characterize the data set. The modes are ordered according to the amount (percentage) of the total variance explained by a mode. The hope is that only a few modes will explain a large fraction of the variance. The approach can be summarized by noting that if we have time series of ice concentrations at M gridpoints (where M is >1000 in our

analyses), we seek a set of N statistically significant modes such that N<<M. As shown later, the sea ice concentration data meets this goal. Modal significance follows North et al. (1982). Finally, we emphasize that modes are a statistical construct from the data set. Often, but not always, the modal structures and their time amplitude functions correspond to a physical mechanism, or they may suggest a physical mechanism.

The modes include weights at each of the original grid points. Grid points with very small weight magnitudes (~0) contribute very little to the information (or variance) contained in that mode, whereas gridpoints whose weights have large magnitude are prominently influencing the spatial structure of that mode. The time amplitude function provides information on how that mode's expression varies through time. If a mode's time amplitude function is very small at a point in time, then that mode's contribution to the data collected at that time is small (and this implies that one or more of the other modes may have been much more prominent than at other times).

We computed the PCs for May, June, July, and August of each year since 1979. We computed these based on daily ice concentrations for each month separately and alternatively, based on the monthly mean maps. The results were virtually identical and we show results from the the latter. Although the modes are a purely statistical construct, they may in fact, have a dynamical or physical basis. We explore this possibility by correlating the time-amplitude functions for significant modes with wind anomalies from the north-central Bering Sea shelf, Bering Strait, and the northeast Chukchi Sea. These correlations were performed with the wind speed and with the zonal and meridional components of the wind velocity.

We also have begun to explore the mechanism(s) that are responsible for subduction by using a simple numerical model (the Rutgers Ocean Modeling System; ROMS) that is configured in a simplistic fashion. The model is configured as a 50-m-deep channel 150 km long in the north−south direction and 150 km wide in a east–west direction. The meridional boundaries are periodic so that the evolving conditions at the northern end of the model are applied at the southern end. The meridional boundaries are solid walls across which there is no mass, heat, or salt transport. The horizontal resolution is 500 m, the vertical grid spacing is 1 m, and the time-step is set at 1 min. Bottom friction is parameterized using a linear bottom friction coefficient of 3×10^{-4} m s^{-1} Vertical and horizontal diffusivities are set to minimal values required to suppress numerical noise. We have conducted two model experiments, with each having a different initial density distribution. In Model 1 (left side of Figure 4), the western and upper half of the water column consists of meltwater (MW) with a density anomaly ($\Delta\rho_1 = \rho_1 - 1{,}000$ kg m^{-3}) of about 26 kg m^{-3} and a corresponding temperature of 0 °C and salinity of 28. Winter water (WW) occupies the lower half of the channel across its entire width and the density anomaly ($\Delta\rho_2$) is 28 kg m^{-3}, a temperature of 0 °C and a salinity of 33. The model's Bering Sea Water (BSW) fills the upper half of the water-column over the eastern half of the channel, with a density anomaly ($\Delta\rho_3$) of 27 kg m^{-3}, a temperature of 5 °C, and a salinity of 30. Thus, Model 1 has a strongly stratified 2-layer structure, including a shallow front in the upper 20 m between the MW and the BSW. As will become evident, this structure mimics that seen in 2013.

The water properties in Model 2 are identical to those in Model 1, but the structure is different and mimics that of 2012. In this model, the 2-layer structure is confined to the western half of the model and unstratified BSW occupies the entire depth over the eastern half of the model.

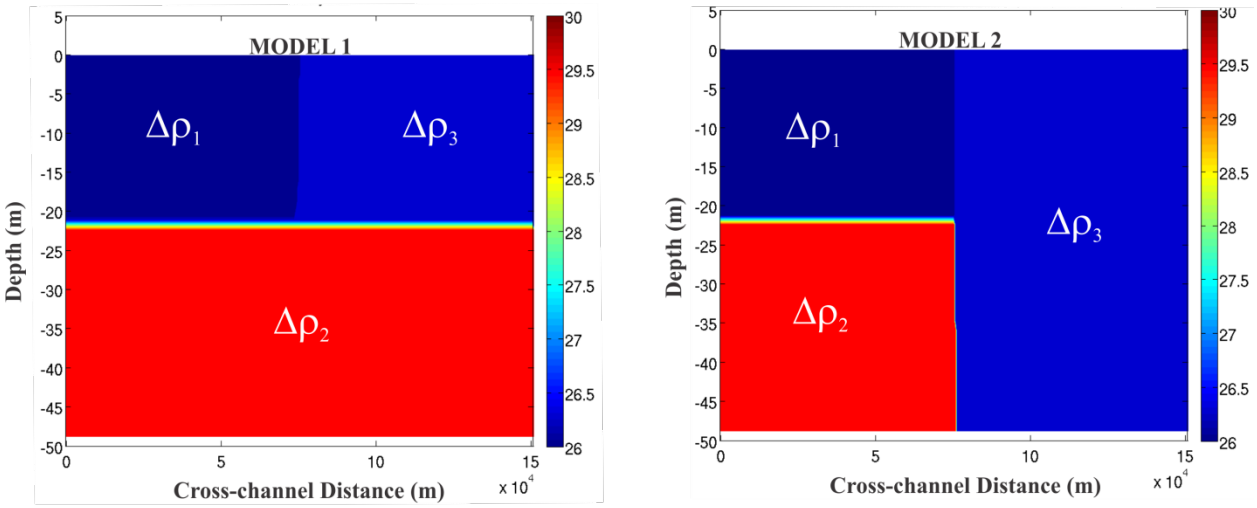

Figure 4. Initial conditions for the two model types used to investigate subduction.

RESULTS

WINDS: 2008–2013

The time-series of 3-hourly wind vectors from 1 June through mid-October from 2008–2013 is shown in Figure 5. In 2008, winds were from the northeast at 5–10 m s^{-1} (10–20 kt) from early July through early October, except for brief periods of a few days of southerly winds scattered throughout the record. In 2009, winds were from the northeast through July, then generally were mild or from the southwest through early September; strong northeasterlies developed by the second week of September and remained so until mid-October. In 2010, moderate northeasterlies prevailed in June, but winds from July through September were much more variable and weaker than in the other years. In 2011, winds were primarily from the northeast from June through mid-October, with only brief interludes of winds from southerly quadrants. In contrast, winds from June through August 2012 blew primarily from southerly quadrants with speeds of 5–10 m s^{-1};

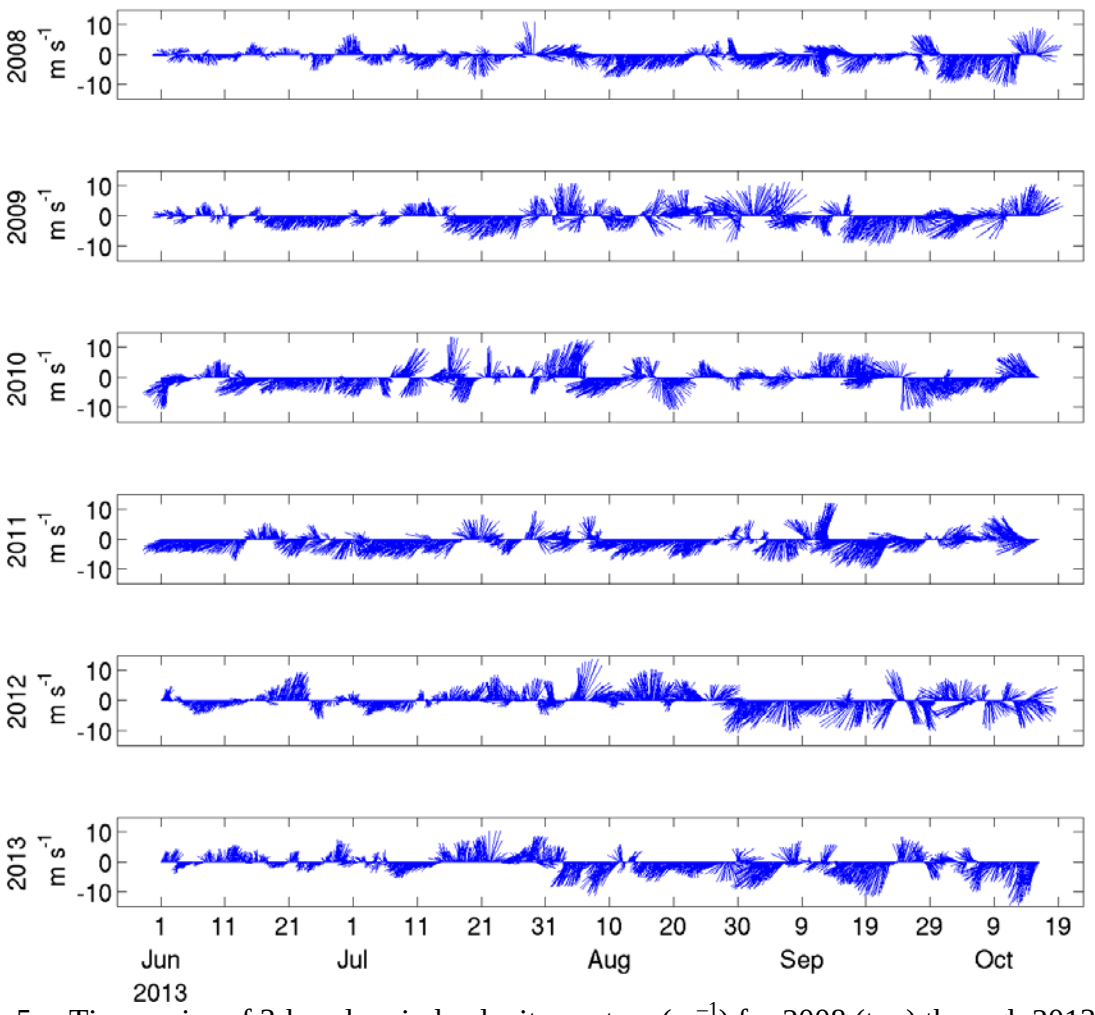

Figure 5. Time series of 3-hourly wind velocity vectors (m^{-1}) for 2008 (top) through 2013 (bottom). The vectors are oriented in the direction toward which the wind is blowing, with True North toward the top of the page. The length of the vector is proportional to the wind speed.

only in early September did winds become northeasterly, with wind speeds generally 5–10 m s^{-1}. In 2013, southerly winds persisted in July, but, beginning in early August, northeasterly winds with speeds of 5–10 m s^{-1} (and occasionally exceeding 10 m s^{-1}) occurred on all except on a few occasions (e.g., 9 September, 24 September, and early October).

The persistence of strong northeasterly winds in 2013 likely has important implications for the regional circulation and hence on the disposition of water properties. We illustrate this point by noting that surface velocities as derived from shore-based high-frequency radars are eastward over the central shelf and northeastward within Barrow Canyon when winds blow toward 220–260°T at <6 m s^{-1} (Figure 6; Weingartner et al., 2012). Under these same conditions, the coastal waters flow offshore of Pt. Lay, and then join the eastward onshore flow over the central shelf. In contrast, for winds blowing toward this same directional sector at speeds >6 m s^{-1}, the flow in Barrow Canyon is southwestward, and the flow offshore of Pt. Lay and over the central Chukchi shelf also is westward (Figure 7)—in effect, the currents reverse direction. Although not shown

here, winds from other quadrants, which occur far less frequently than do winds from the northeast, generally promote northeastward flow in Barrow Canyon and along the coast and eastward flow toward the coast across Klondike and from the Central Channel (Weingartner et al., 2013a, Weingartner et al., 2013b).

These mean surface velocity depictions are consistent with limited observations of satellite-tracked drifter deployments on the Chukchi Sea shelf as reported by Weingartner et al. (2014). For example, in 2011, drifters released in the Statoil and Burger study area in mid-August drifted eastward and into Barrow Canyon (Figure 9) over the next month even though winds were primarily from the northeast, but at average speeds of <5 m s^{-1}. Similarly, in August 2012, drifters deployed both southeast and southwest of Hanna Shoal in August also moved eastward and entered Barrow Canyon (Figure 10). In contrast, drifters released offshore of Pt. Lay in mid-August 2013 moved offshore (westward) as far west as the Central Channel throughout August (Figure 11). This westward drift was consistent with a coastal-upwelling response to northeasterly, alongshore winds (Figure 5). These drifters moved westward at speeds of 10–30 cm s^{-1} until about 8 September, when they reached the Central Channel

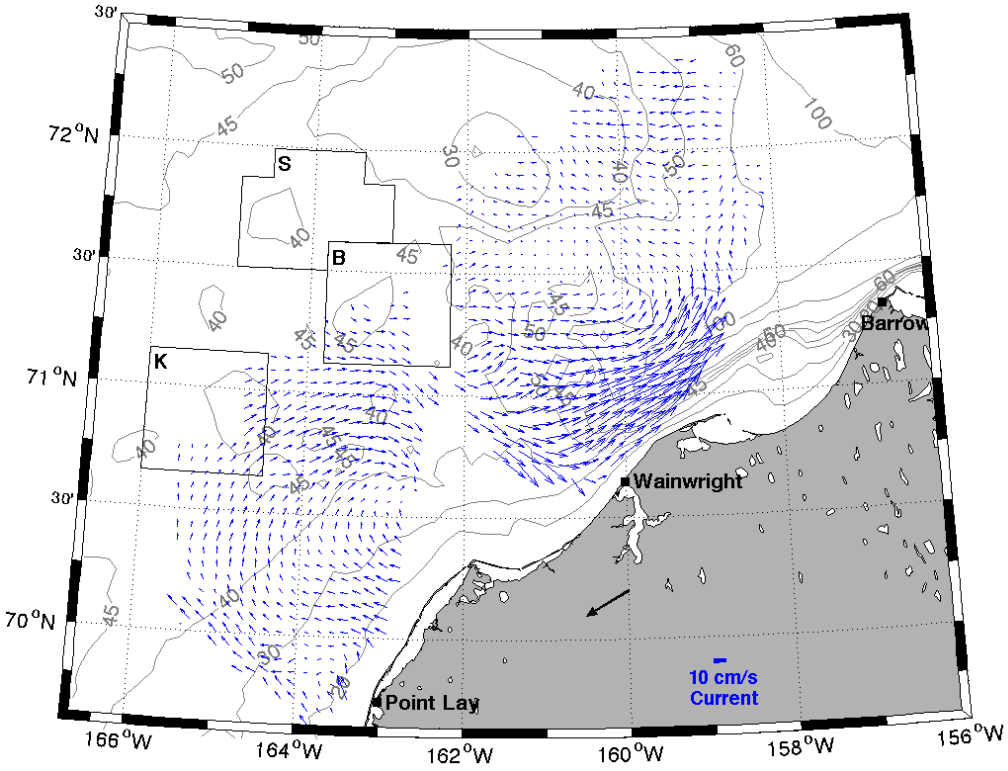

Figure 6. Mean surface currents for periods when winds blew toward 220–260 °T at wind speeds less than 6 m s^{-1}.

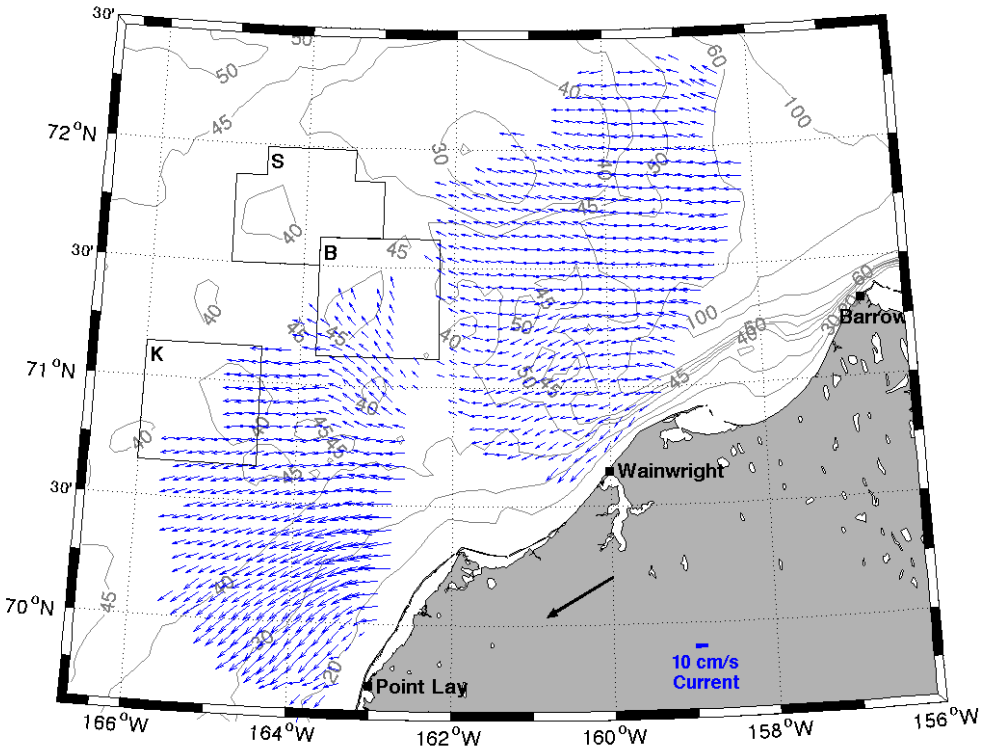

Figure 7. Mean surface currents for periods when winds blew toward 220–260°T at wind speeds greater than 6 m s^{-1}.

From there, they then moved northward in the Channel through 18 September, during a period of relatively weak northeasterly winds. These winds then intensified through 24 September and were strong enough to drive the surface flow westward. The winds relaxed somewhat in late September, and the drifters resumed their northward set until the end of this record. The temperature traces clearly indicate northward movement of warm water through the Central Channel (Figure 10, upper panels). This pattern is consistent with the Central Channel being an important pathway by which warm BSW makes its way onto the northeastern Chukchi shelf.

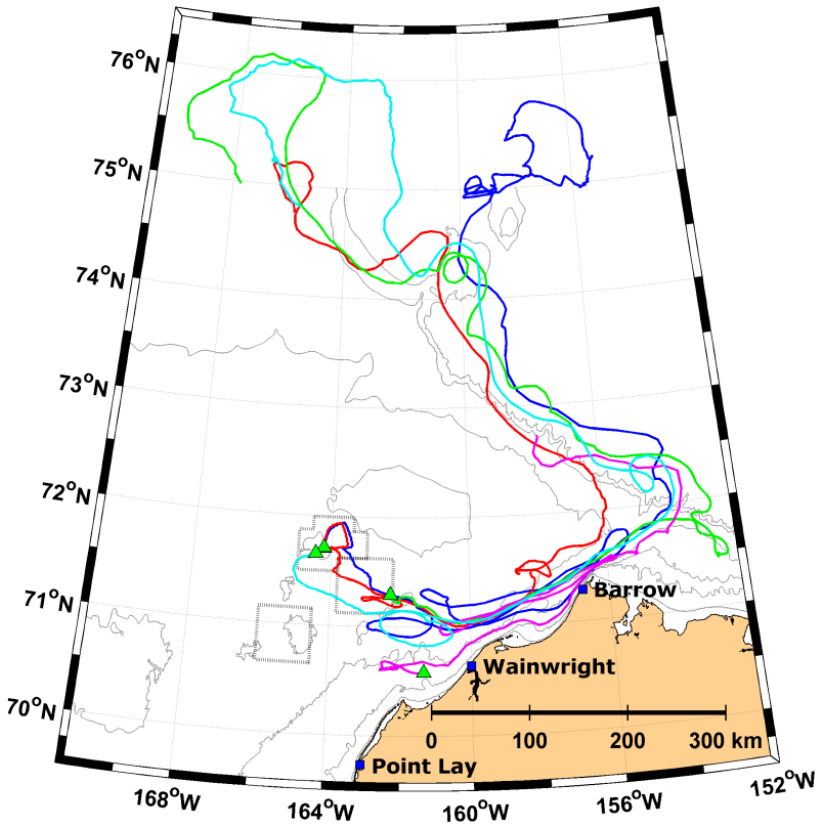

Figure 8. Trajectories of satellite-tracked drifters deployed in mid-August 2011; deployment locations are denoted by triangles. These drifters moved eastward between mid-August and mid-September, then moved northeastward through Barrow Canyon. (From Weingartner et al., 2014).

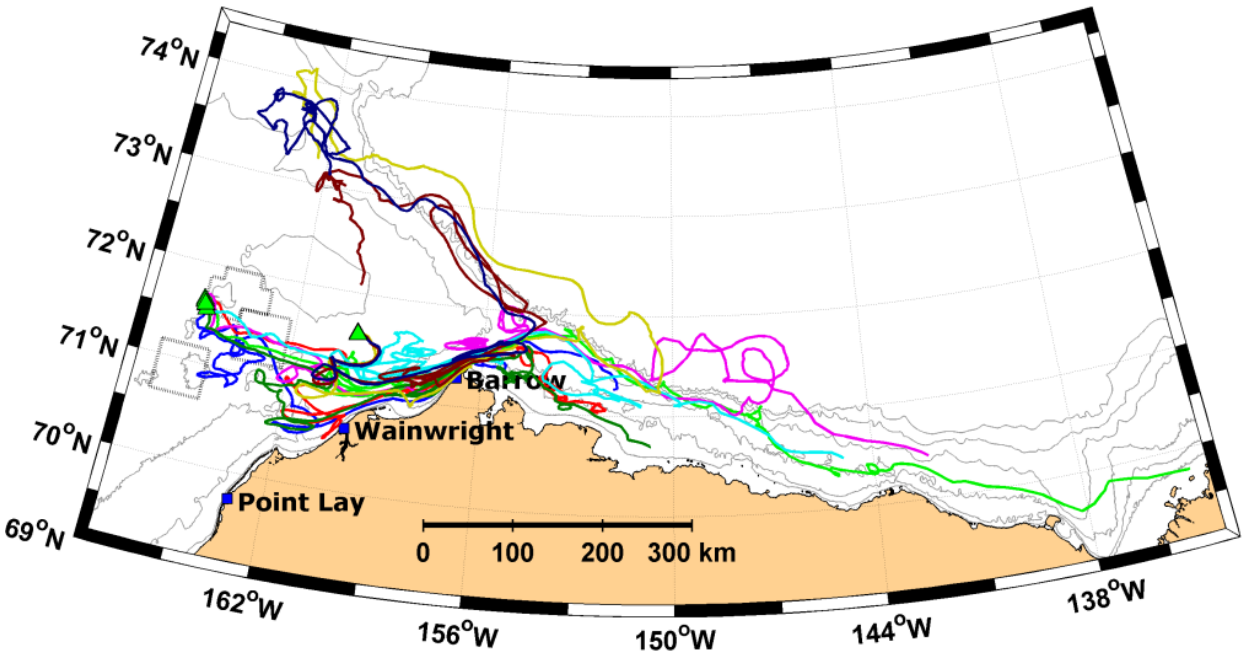

Figure 9. Trajectories of satellite-tracked drifters deployed in August 2012; deployment locations are denoted by triangles. These drifters moved eastward between mid-August and mid-September, then moved northeastward through Barrow Canyon. (From Weingartner et al., 2014).

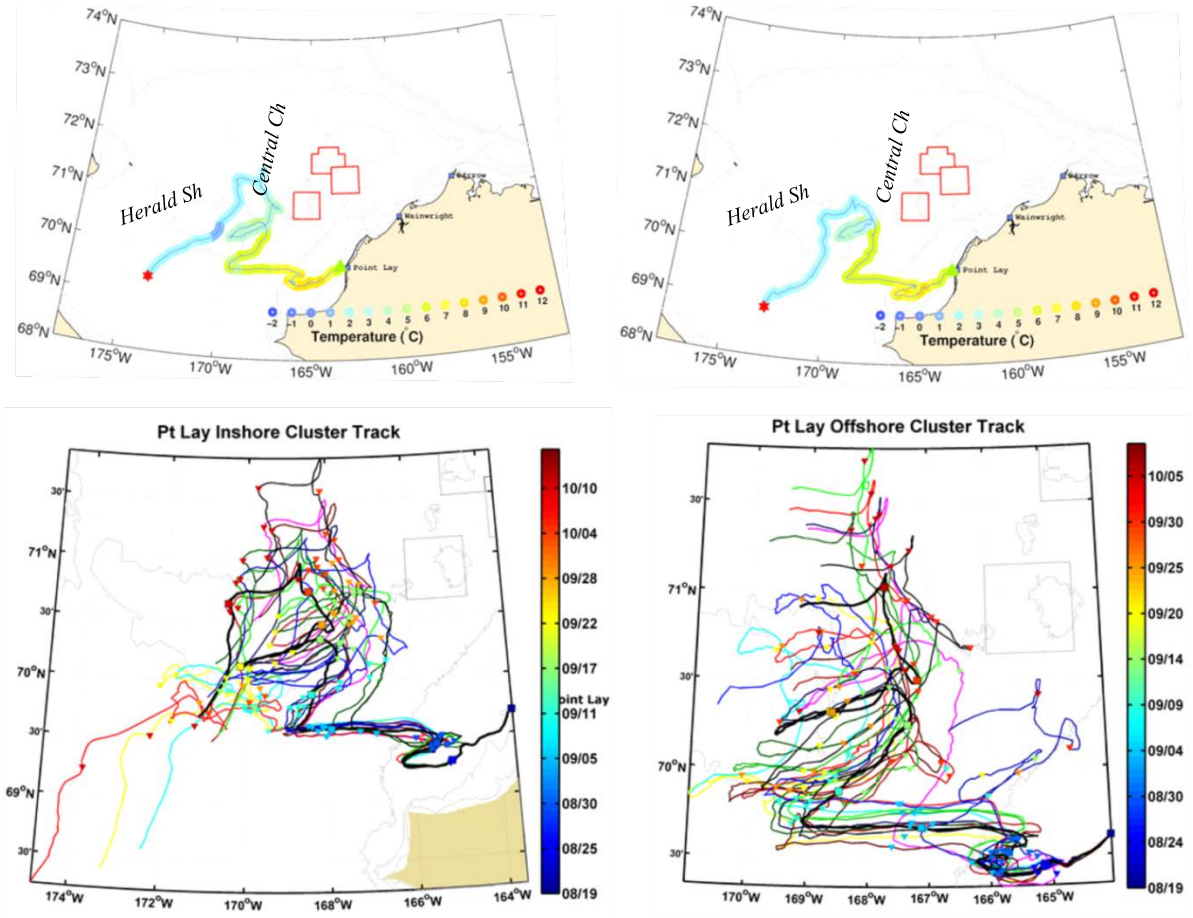

Figure 10. Satellite-tracked trajectories of drifters deployed offshore of Pt. Lay, 19 August 2013. Two clusters, one inshore and one offshore, each containing 13 drifters, were deployed about 10 km apart. An example trajectory from the inshore (offshore) cluster is shown in the upper panels. The color-coding along the trajectories corresponds to the sea-surface temperature in the legend. The lower panels show the trajectories of all drifters deployed in each cluster; the heavy black curve in these panels traces the center of mass of the cluster. Colored symbols along the trajectory pathways correspond to the date legend in the sidebars. Red asterisks denote the last good drifter position fix. (From Weingartner et al., 2014).

Drifters released offshore of Wainwright on 24 August (of which a subset is shown in Figure 11) made several southwest–northeast excursions through mid-October before either exiting through Barrow Canyon or drifting to the southwest over the Chukchi shelf. This brief review suggests that, in contrast to the pattern seen in previous years, the 2013 August surface circulation over the northeastern and central Chukchi shelf was quite different and a consequence of the strong northeasterly winds that prevailed over the shelf in August.

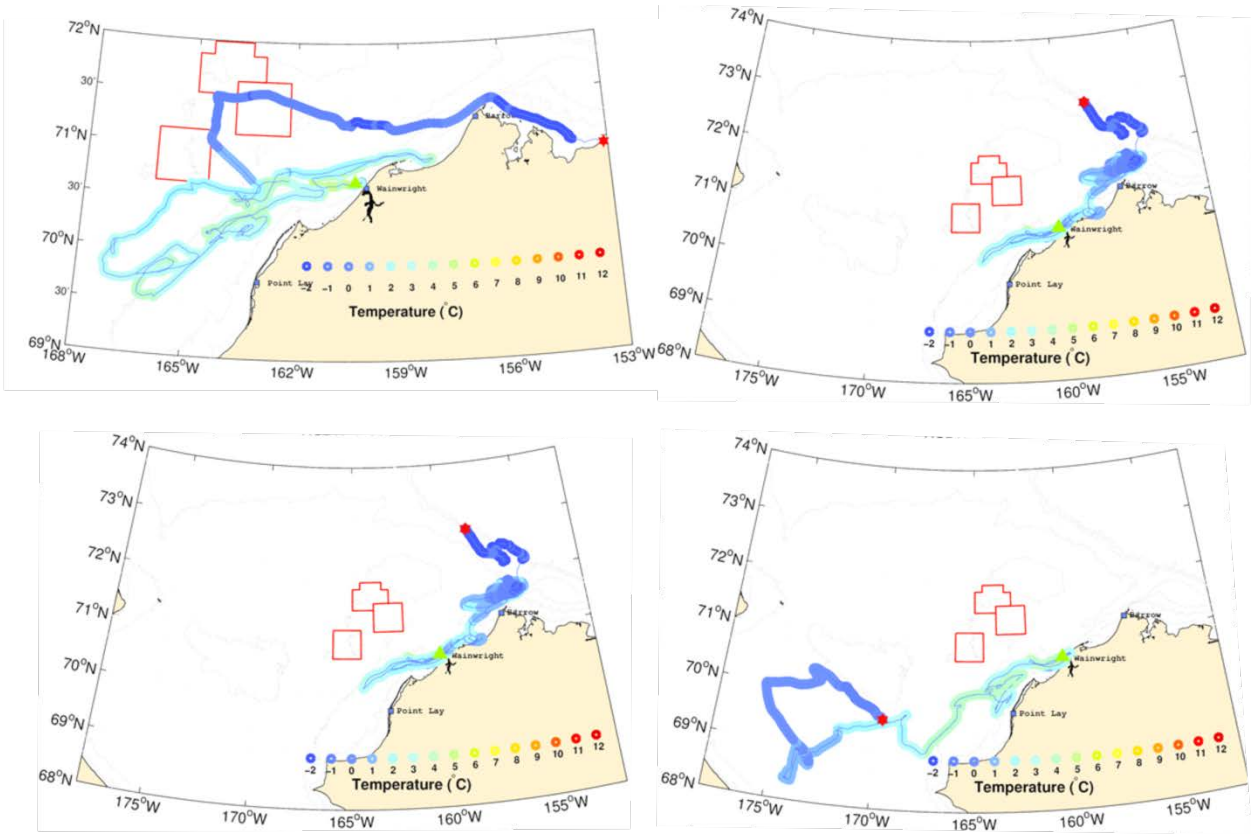

Figure 11. Satellite-tracked trajectories of a subset of drifters deployed offshore of Wainwright, 24 August 2013. Color-coding along the drifter trajectory corresponds to the sea-surface temperature according to the legend in each plot. Red asterisks denote the last good drifter position fix. (From Weingartner et al., 2014).

SEA ICE CONCENTRATIONS

Ice-concentration maps for May, June, and July 2013, derived from data obtained by the Special Sensor Microwave Imager (SSMI) satellite sensor and processed to Spreen et al. (2008). The time sequence of maps provides a broader perspective of the seasonal evolution in sea ice retreat over the Chukchi shelf prior to the 2013 vessel surveys (Figure 12). In 2013, substantial ice retreat began in Bering Strait by the third week of May, which was similar to the start of the retreat in 2012 but ~2 weeks later than the retreats of 2008–2011. The reasons for this sluggish start are not clear but may have been due at least partially to the extensive ice cover formed over the Bering Sea during the previous winter. Ice-retreat occurred slowly at first, with the ice edge reaching ~69 °N only in mid-June, but it then progressed more rapidly. Hence by early July, the major ice embayments within Herald Canyon, the Central Channel, and Barrow Canyon were evident. By late July, much of the western Chukchi Sea was ice-free, but heavy concentrations of ice remained over the northeast shelf, particularly in the area atop and to the east of Hanna Shoal. As shown below, ice lingered in the northeast Chukchi Sea over Hanna Shoal through August but was not detectable by the SSMI in September.

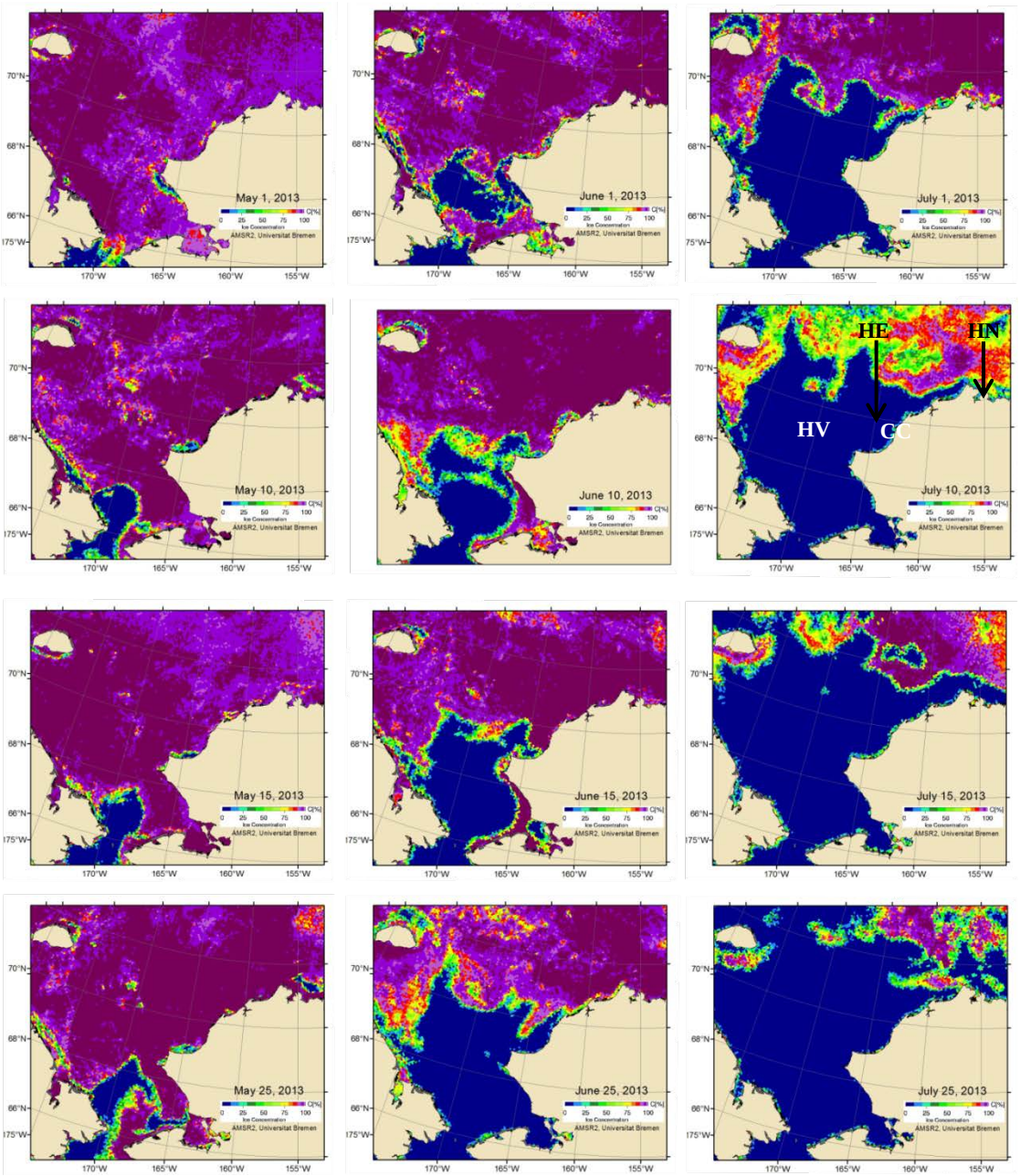

Figure 12**.** Sea ice concentration maps in 2013 for May (left), June (middle), and July (right). The labels on the July 15 map refer to Hanna (HN) and Herald (HE) shoals, the Central Channel (CC), and Herald Valley (HV).

There are three principal modes of ice-retreat in May (Figure 13). The dominant mode (PC1, which accounts for 46% of the variance in May ice concentration) corresponds to ice-retreat and/or ice-melt proceeding northward from Bering Strait. The second mode (PC2, which accounts for 27% of the variance) depicts a pattern in which changes in ice concentration along the northwestern coast of Alaska are out of phase with changes in concentration along the northern coast of Chukotka. The third PC (~7% of the variance) is not statistically significant. The time-amplitude function (lower panel of Figure 13) indicates that PC2 had large amplitudes

in 2008 and 2010 (with reduced ice concentrations along the Alaska coast), whereas in 2009 this mode was large but anti-phase (heavy ice concentrations in Alaska but light concentrations along Siberia). When viewed over the entire time-series, the largest amplitudes in PC1 occurred in 1980–1985 and 1995–2005, while the PC2 amplitudes for the 2008–2013 pentad were among the largest observed for this mode. In addition, the PC2 amplitudes have an approximate 2–4-year periodicity. Correlations between the May PCs and the monthly wind velocity component anomalies indicate that PC1 is positively correlated with both the east–west (r = 0.43) and north–south (r = 0.44) wind components in Bering Strait and over the central Bering shelf, where the correlation coefficients are smaller, but nevertheless significant. The signs of these correlations are consistent with the hypothesis that wind-induced forcing in the Strait and over the Bering shelf affect northward transport and, therefore, the northward flux of heat through the Strait (Danielson et al., in press). The PC2 time series is significantly correlated with winds over the northeastern Chukchi Sea, with winds from the east (west) and or south (north) leading to reduced (increased) ice concentrations along the northwest Alaskan coast. The correlation coefficients (r) are 0.68 for the zonal wind component and 0.64 for the meridional wind component.

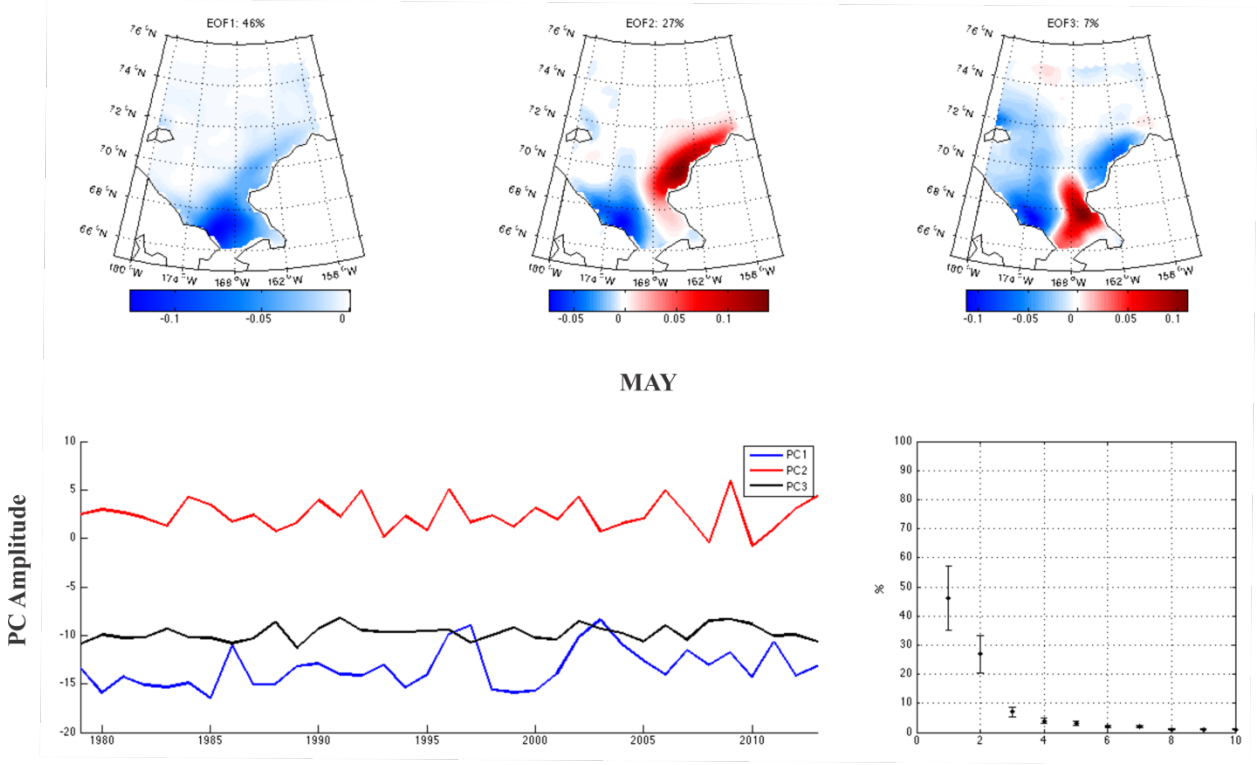

Figure 13. PC summary for May. Upper panels show the spatial structure associated with the first three modes (PC1–PC3), the lower-left panel shows the time-amplitude function of the modes, and the lower-right panel shows the percent variance and 95% confidence limits (vertical bars) of the modes.

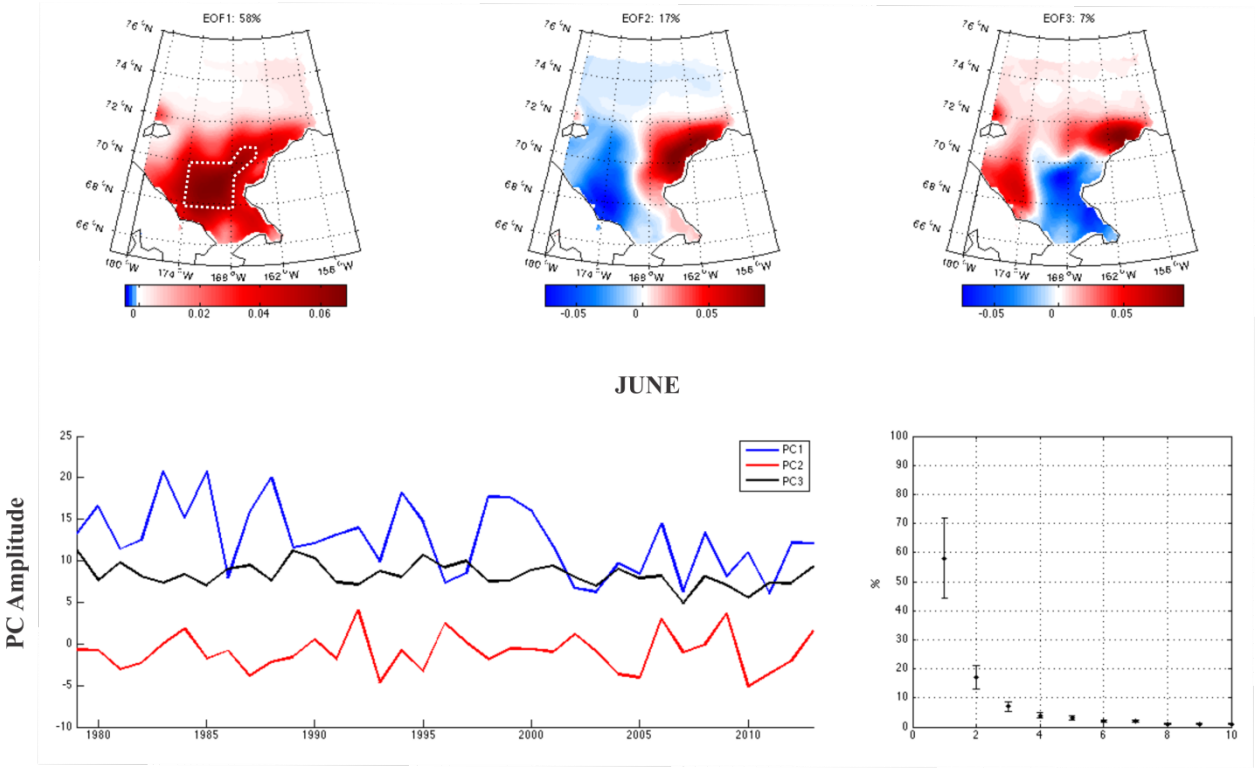

Figure 14. PC summary for June. Upper panels show the spatial structure associated with the first three modes, lower left shows the time amplitude function of the modes, and lower right shows, the percent variance and 95% confidence limits (vertical bars) on the modes. The white dotted line in the upper-left panel outlines the region of maximum spatial variability in the first mode.

For June, the PCs (Figure 14) indicate overall similar patterns to those seen in May (Figures 13). The first PC, which describes variability in northward ice retreat, accounts for 58% of the variance in ice concentration. The modal weights indicate that maximal variability occurs in the area outlined by the dotted white lines (i.e., over Hope Sea Valley, with an extension to the northeast in the Central Channel). The spatial structure of PC1 also shows that the patterns of ice retreat are beginning to outline the principal flow pathways (in Herald Canyon, the Central Channel, and the west coast of Alaska). The PC1 amplitude function indicates that this mode is highly variable from year-to-year. However, PC1 variability has decreased (by ~ 1/3) over the past decade from the pattern seen in the first 2 decades, with this decrease presumably related to the decrease in June ice concentrations over the southern Chukchi shelf. There also is a ~2–4 year periodicity in the amplitude function that is evident even as the overall variability in PC1 has decreased through time. PC1 is uncorrelated with the winds over the Bering and Chukchi shelves, but it is significantly correlated with the zonal and meridional winds in the Chukchi Sea (r = 0.37 and 0.24, respectively). This set of correlations suggests that other atmospheric influences (solar radiation) and/or ocean-based processes (heat advection and/or mixing) are governing this mode's variability. The June PC2 is similar to PC2 of May in having an anti-phase relationship between the eastern and western Chukchi Sea and in that this mode's variability has been greater over the past decade than it has been in the previous 25 years. As with PC2 of May, the PC2 of June shows significant correlations with the east and north

components of the wind (r = 0.42 and r = 0.54, respectively) over the Chukchi Sea. PC3 is not statistically significant.

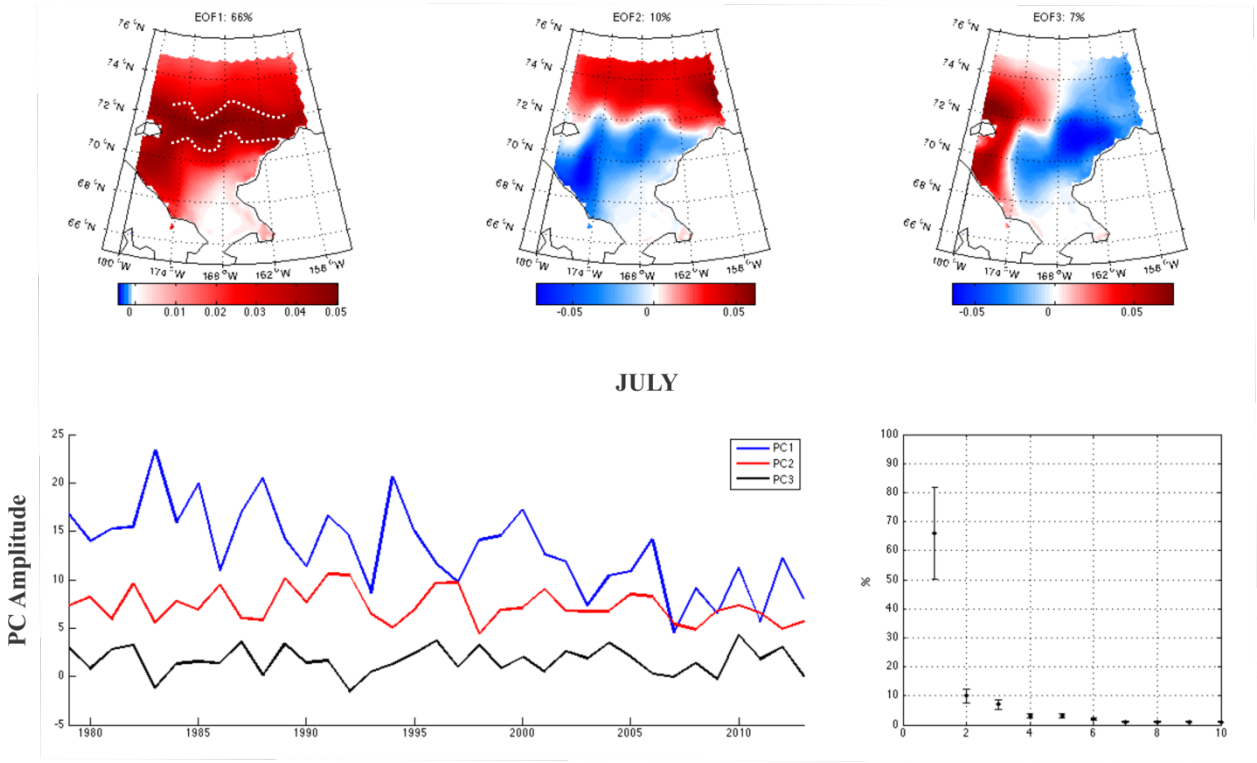

Figure 15. PC summary for July. Upper panels show the spatial structure associated with the first three modes, lower left shows the time amplitude function of the modes, and lower right shows, the percent variance and 95% confidence limits (vertical bars) on the modes. The white dotted line outlines the region of maximum spatial variability in the first mode.

In July, the overall patterns concern the retreat of ice on and off the northern Chukchi shelf,. Only the first PC is significant, accounting for 66% of the variance in ice concentration (Figure 15). Its region of maximal variability extends in a zonal belt between 70.5°N and 72°N (outlined by dotted white lines in the upper-left panel of Figure 15). The time-amplitude function indicates that this mode is highly variable from year-to-year but that the variability has decreased with time, especially over the past decade. Again, the amplitude of the time-series has a ~2–4-year periodicity; as was seen in June, this periodicity is apparent even as the variability of PC1 has decreased. There is no significant correlation between PC1 and wind velocities; however, it is significantly correlated (r = 0.43) with wind speed.

In August, only the first PC is significant (Figure 16), accounting for 72% of the variance in ice concentration. The region of maximum variability is north of ~72 °N, and the southern limit of this region of maximum variability tends to align with the principal flow pathways along which Bering waters flow northward. There are two time scales evident in the amplitude time series. The first occurs at the 2 – 4 year period as previously identified. However, the amplitude of this signal is modulated by a longer-term and/or rather abrupt decrease in variability that occurred

between 1995 and 2000. The only significant correlation (r = 0.42) between this mode and wind velocity is with the east–west component of wind over the northeastern Chukchi Sea shelf. The sign of the correlation is such that eastward winds are associated with a decrease in ice cover. There also is a positive correlation (r = 0.56) between PC1 and wind speed.

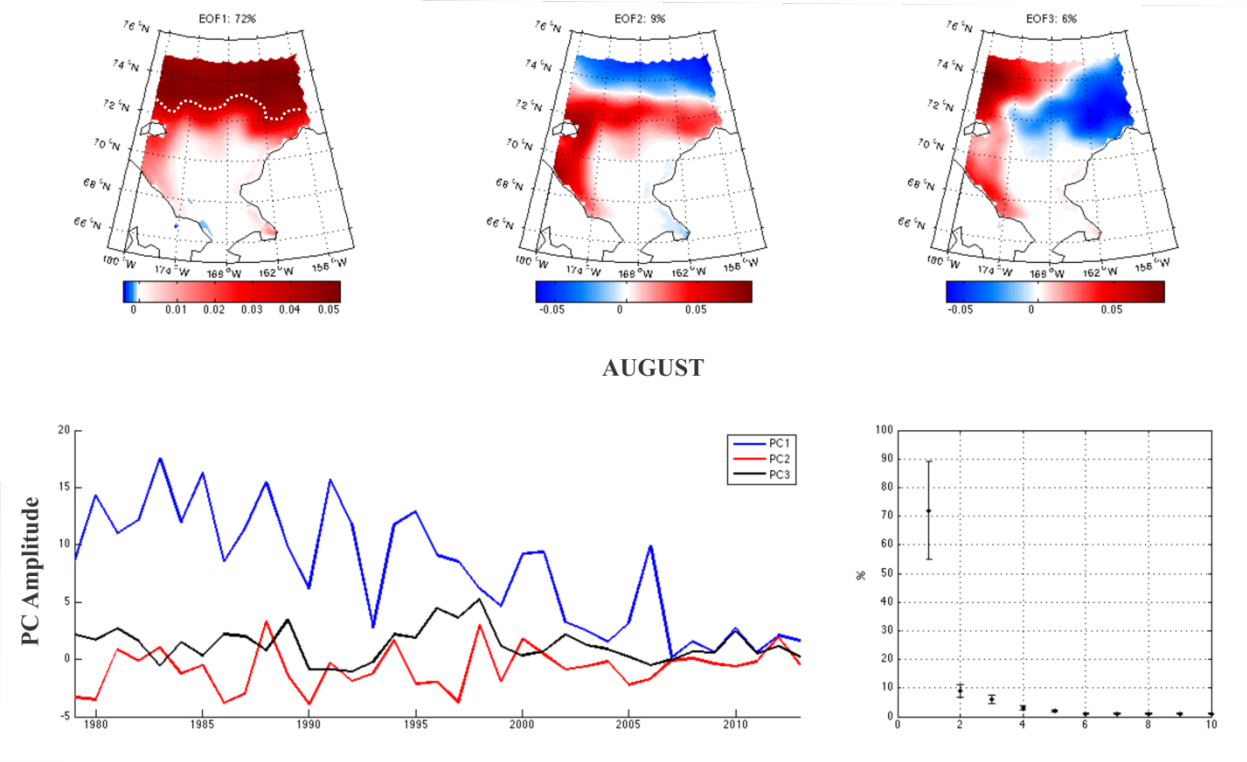

Figure 16. PC summary for August. Upper panels show the spatial structure associated with the first three modes, lower left shows the time amplitude function of the modes, and lower right shows, the percent variance and 95% confidence limits (vertical bars) on the modes. The white dotted line outlines the southern extent of the region of maximum spatial variability in the first mode.

We summarize the preceding results as follows. The modes that characterize variability in monthly ice retreat change seasonally. Two modes explain most of the variance in ice concentration in both May and June. The dominant mode (PC1) is the northward, or meridional, decrease in ice concentration, whereas the secondary mode (PC2) is associated with an east–west anti-phase relationship in ice distribution across the Chukchi shelf. The latter pattern is significantly correlated with winds over the northeastern Chukchi Sea shelf. In July and August, only the meridional mode is statistically significant. The PC1 modal amplitudes of June, July, and August capture two time-scales of variability: a biennial periodicity and a multi-decadal trend in reduced variability. The first trend is significantly correlated with winds over the northeastern Chukchi Sea, whereas the latter trend reflects the long-term decrease in summer ice-concentrations in the Arctic. The correlation suggests that the biennial variability is atmospheric in origin, although we have not identified the source. The biennial variability also provides some hope for making limited predictions of seasonal (summer) Chukchi Sea ice concentrations insofar as it suggests that the trend in June ice cover will continue through August (at least) and that alternating years will have reduced (or greater) ice concentrations than previous years. Note

that this predictability pertains to the entire Chukchi shelf; hence, it does not imply that accurate predictions of ice-retreat can be made over more restricted portions of the shelf (e.g., in the area of potential hydrocarbon exploration). Additional work along these lines is needed to identify the cause of the quasi-biennial periodicity and to determine the spatial scales over which the prediction applies.

We next consider the evolution of sea-ice concentrations over the northeastern Chukchi Sea, including the survey areas, for the period of early August–early September 2013. From 1 to 8 August (Figure 17, top) a broad tongue of ice of varying concentrations protruded to the southwest over the northeastern Chukchi shelf. The ice edge was compact on 1 August, probably because of the southwesterly winds of late July. By 4 August (Figure 17, middle), the ice-edge was more diffuse, consistent with the northeasterly winds that arose in early August. By 8 August (Figure 17, bottom), the ice tongue extended farther southward and westward between 160 °W and 165 °W, although open water was present in Barrow Canyon. On all of these days, the heaviest concentrations of ice were located over Hanna Shoal, centered at 72 °N and between 162 °W and 164 °W. From 11 to 18 August (Figure 18), ice eroded/retreated along the western side of Hanna Shoal (between 165 °W and 170 °W), presumably due to the influence of warm waters flowing northward in the Central Channel. Although the area to the east of Hanna Shoal was ice-free or had reduced ice concentrations at this time, tongues of ice extended eastward toward and northeastward along Barrow Canyon, even though the winds were from the northeast. These streamers, which were prominent on 15 and 18 August, may arise due to the eastward flow from the central shelf toward Barrow Canyon. Overall, the ice-edge remained fixed in position during this period and was oriented from the southeast (71 °N, 160 °W) to the northwest (71.5 °N, 165 °W). Although the location of the ice-edge changed little, the maps suggest that the ice-edge became more diffuse and convoluted than it had been previously (e.g., on 11 August). These convolutions appear to be associated with eddy activity along the ice-edge as discussed later. The ice eroded quickly over the next 10 days (Figure 19), especially along the eastern side of Hanna Shoal. Even over the Shoal itself, ice concentrations still were heavy but began to decrease substantially. Nevertheless, the ice-edge still extended into the Statoil and Burger study areas and remained there into early September (Figure 20). Thus in many ways, the ice distribution in August 2013 was similar to that of 2012. The persistent ice-cover over Hanna Shoal serves as a reservoir of freshwater that exerts a profound influence on the stratification and presence/location of fronts over the shelf, as discussed next.

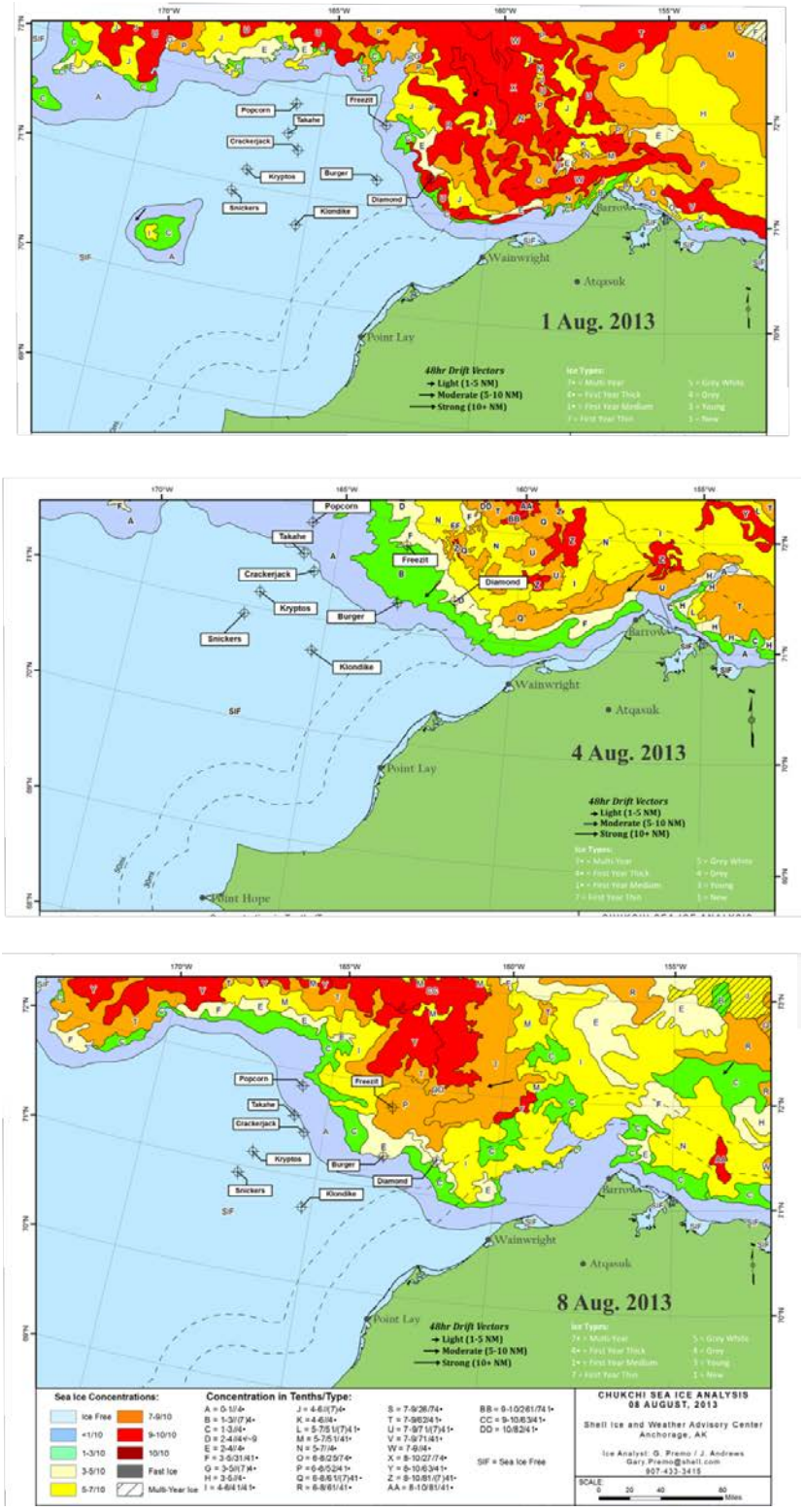

Figure 17. Maps of sea-ice concentration in the northeast Chukchi Sea on 1 (top), 4 (middle), and 8 (bottom) August 2013. Map is courtesy of Shell Ice and Weather Advisory Center.

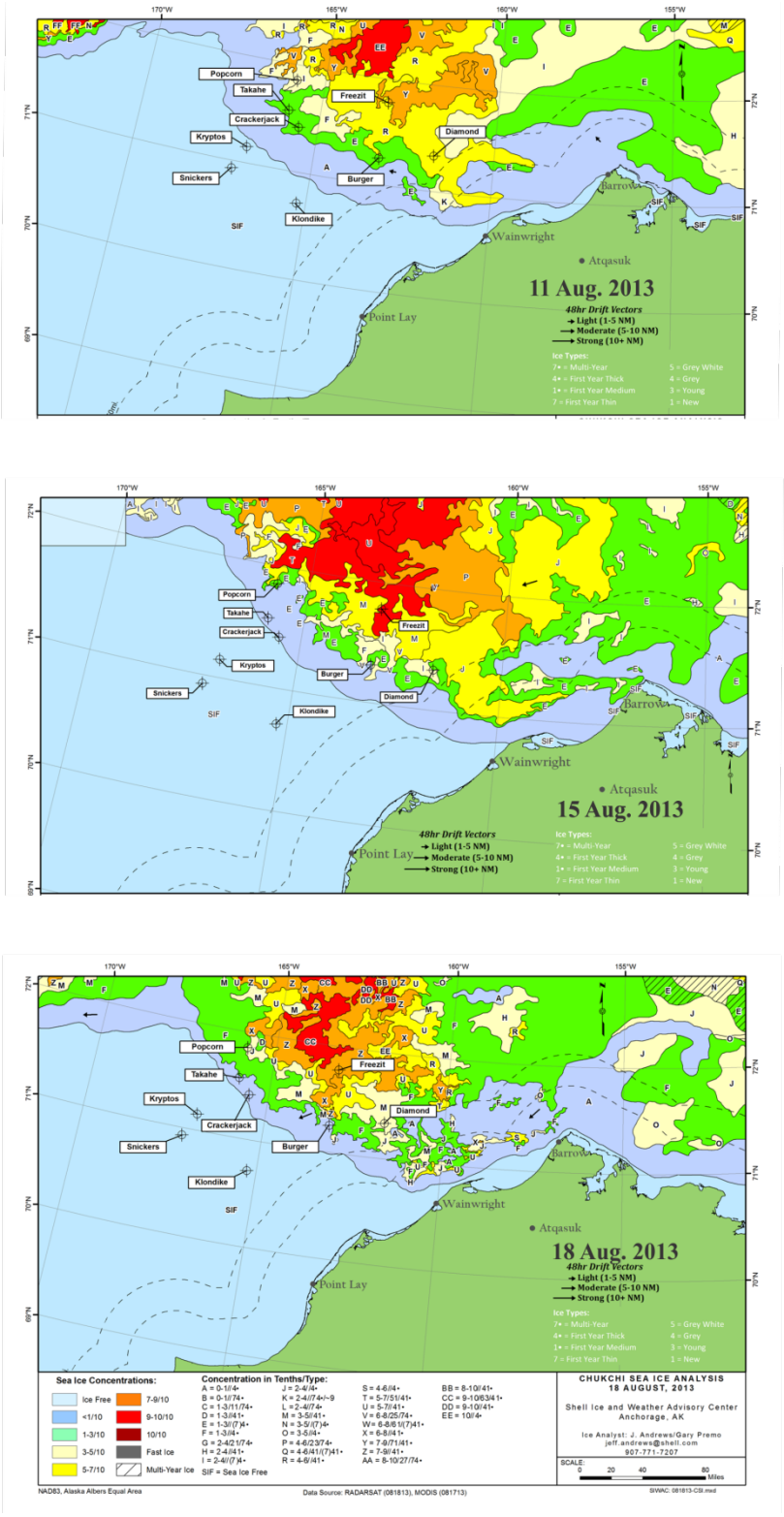

Figure 18. Sea ice concentration map in the northeast Chukchi Sea on 11 (top), 15 (middle), and 18 (bottom) August 2013. Map is courtesy of Shell Ice and Weather Advisory Center Science.

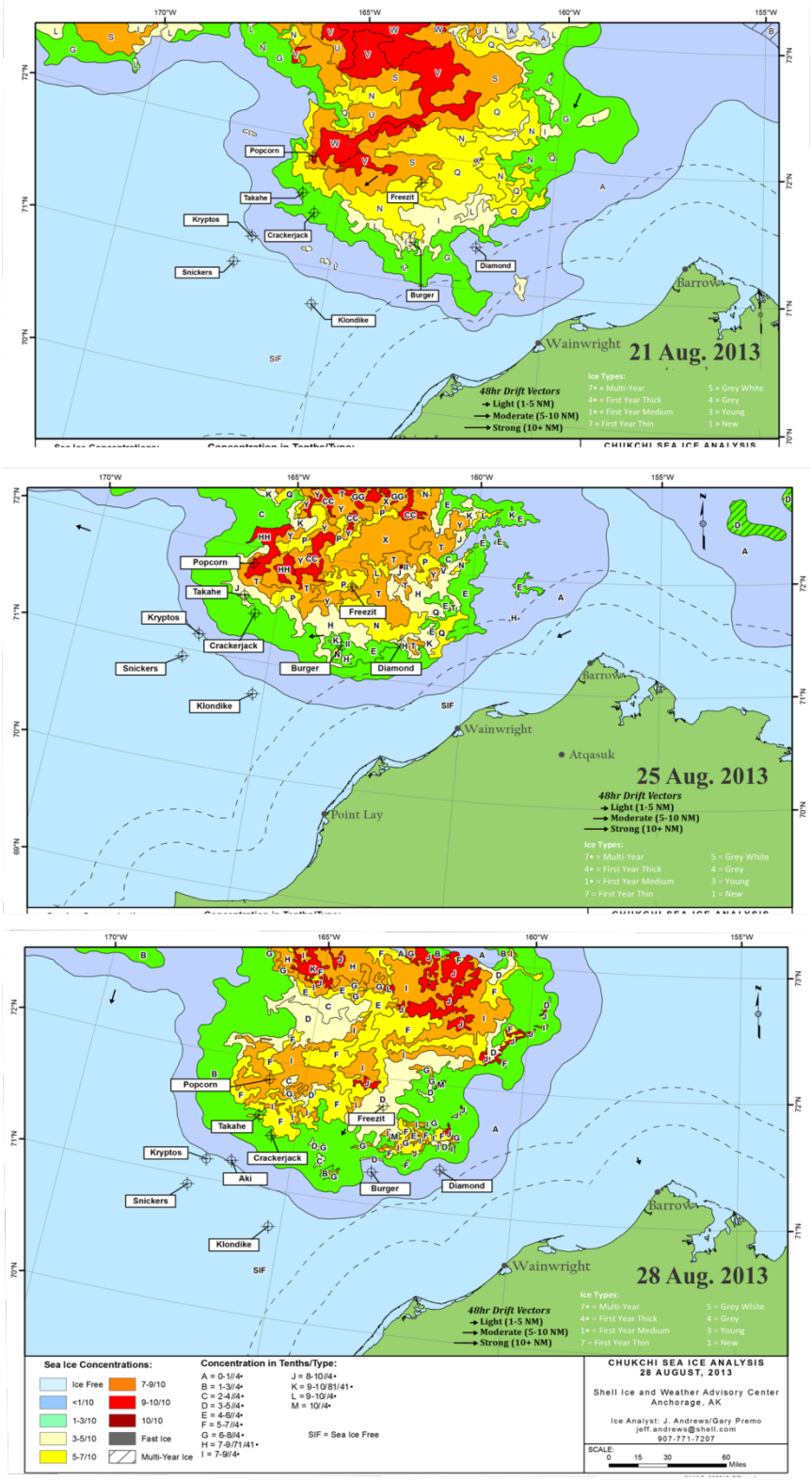

Figure 19. Sea ice concentration map in the northeast Chukchi Sea on 21 (top), 25 (middle), and 28 (bottom) August 2013. Map is courtesy of Shell Ice and Weather Advisory Center Science.

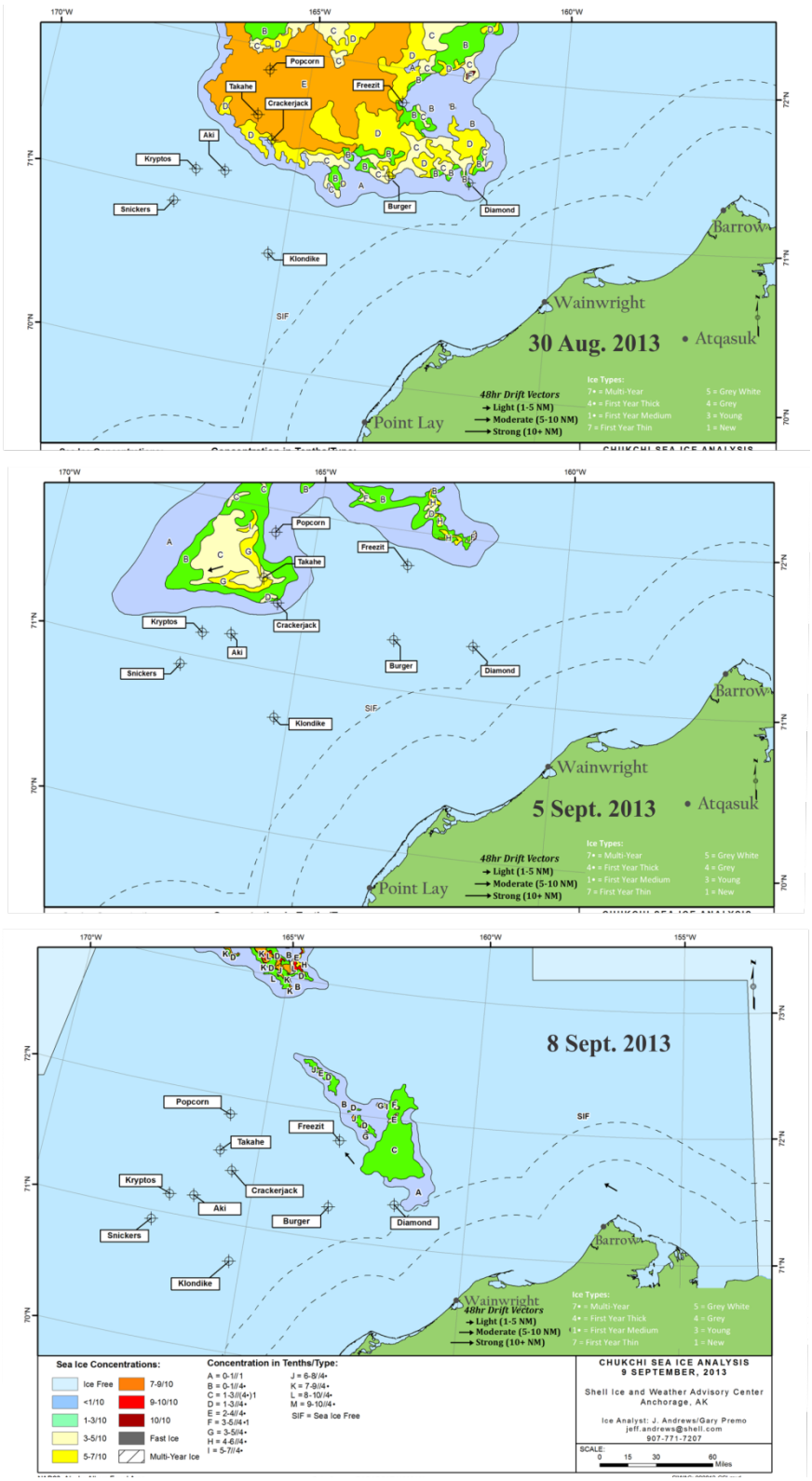

Figure 20. Sea ice concentration map in the northeast Chukchi Sea on 30 August (top), 5 (middle), and 8 September (bottom) 2013. Map is courtesy of Shell Ice and Weather Advisory Center Science.

HYDROGRAPHY IN 2013

Before presenting the spatial distribution of temperature (T) and salinity (S) along the CTD transects, we first describe the various water-masses found in the survey areas, based on T/S diagrams (Figure 21). These scatterplots depict the T and S characteristics at each 1-m-averaged CTD sample from all casts in the study area. The data are segregated into stations during the 11–23 August and the 20 September–8 October cruises.

The overall distribution of data points is similar to that found in previous years in consisting of cool (<2 °C) and fresh (<30) Meltwater (MW), a remnant of very cold (<2°C) and salty (>32.5) Winter Water (WW) from ice formation on the Bering and/or Chukchi shelves during the previous winter, and an intermediate grouping of warm (>2°C) and moderately saline (30–32.5) Bering Sea Water (BSW) that arrived in the summer from the Bering Sea. There also are water types having characteristics between these basic groupings, indicative of mixtures of the basic water-masses. These basic groupings are evident on both cruises.

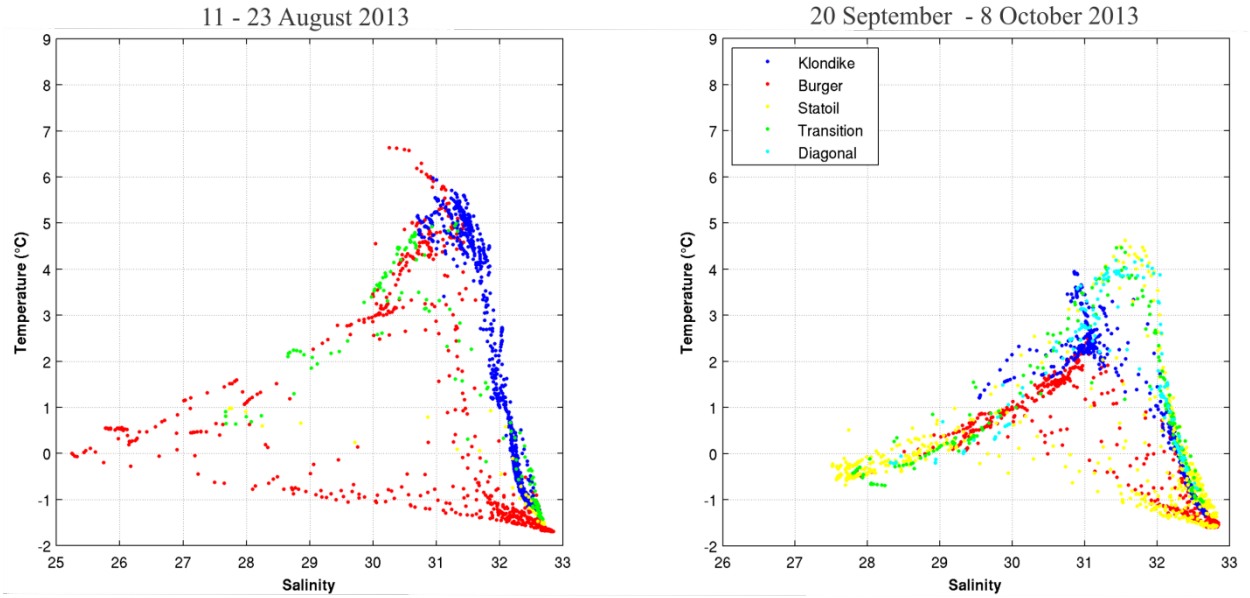

Figure 21. Temperature–salinity diagrams for the 11–23 August 2013 cruise (left) and the 20 September–8 October 2013 cruise (right).

Several general patterns are evident in the scatterplots. First, during the 11–23 August, water in Klondike consisted primarily of BSW and WW, with mixtures evident between these two water masses. Salinities in Klondike ranged from ~31 to 32.5, and temperatures ranged from –1.5 °C to 6 °C, so the stratification here is due primarily to temperature and not salinity. Second, Statoil and Burger contain MW, BSW, and WW, but the stratification is primarily a function of salinity. (Note that there were few stations occupied in Statoil on this cruise due to the heavy cover of sea ice.) Third, although the basic water-mass types were present on both cruises, the range in both temperature and salinity decreased between the two cruises. The decrease in the warmest temperatures reflects seasonal cooling by heat loss to the atmosphere that typically begins in September (Weingartner et al. 2013a), plus mixing of warmer BSW with cooler waters. The decrease in the salinity range also reflects horizontal and vertical mixing, which tends to

homogenize the water masses. Both processes would have removed the freshest waters from the area. There appears to have been very little change in the amount of WW in the area as this is present in all study areas on both cruises. Fourth, although the salinity of the MW diminished between the two cruises, MW was evident at Klondike on the second cruise, implying that this water mass had been advected into the region between the two cruises. Hence, MW and WW persisted throughout the entire season at all locations. In all previous years except 2008, there was a gradual decrease from summer through fall in the frequency of occurrence and spatial extent of MW and WW as these water-masses were replaced by BSW. Finally, in 2013, the waters were cooler than in all previous years except 2008: maximum temperatures were ~6.5 °C in 2012 and 2013, whereas temperatures exceeding 7 °C were common in earlier years. As a further contrast among years, we include the T/S diagram from 2011 (when virtually no MW was present; Figure 22). As noted in previous reports, 2011 was unusual in that stratification over the entire sampled region was generally established by vertical temperature gradients, given the narrow salinity range of ~30–32.5 (i.e., similar to what was seen in Klondike on the August cruise). In 2012, the stratification was largely determined by salinity except in Klondike and the shelf south of ~71 °N. In 2013, the stratification in Klondike was largely a function of temperature during the August cruise but a function of both temperature and salinity during the second cruise.

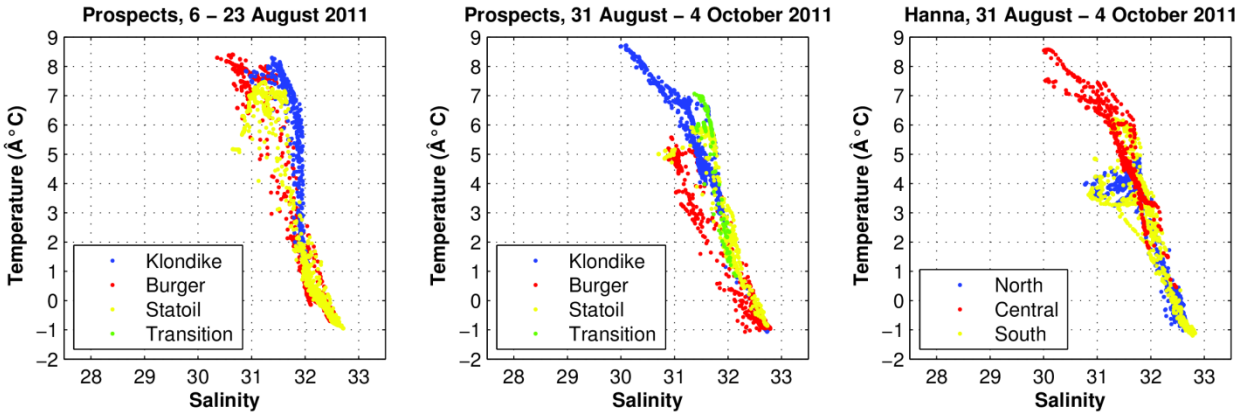

Figure 22. Temperature–salinity diagrams for each survey conducted in 2011. The left and middle panels are the T/S plots for the study-area boxes, and the right panel is for data collected during the second cruise at stations outside of the study-area boxes. (Figure from Weingartner et al., 2013c.)

WATER-PROPERTY DISTRIBUTIONS

We next investigate the spatial distributions of temperature, salinity, density, fluorescence, and beam-transmission as a function of distance and depth (pressure) along a number of transects across the region. Vertical sections similar in location to those constructed in previous years are shown separately for the 11–23 August 2013 cruise (Figures 22–23) and for the 20 September–8 October cruise (Figures 24–29).

The first section from Cruise WWW1302 extends eastward along the northern boundary of Klondike and the southern boundary of Burger (Figure 23). This section consists of a strongly

stratified ~5 m thick pycnocline centered at a depth of ~15 m. The surface layer was well-mixed, with temperatures ranging between 4 and 6.5 °C but generally at ~5.5 °C; salinities generally were ≤31. Below 20 m, the water-column also was well-mixed, with temperatures and salinities typically <–1 °C and ~32.5, respectively. There were no strong horizontal temperature or salinity gradients (fronts) along this section; hence, horizontal density gradients also were weak. Thus, the upper 15 m (mixed layer) were occupied by BSW, whereas the bottom layer consisted of WW. Fluorescence was weak except for a small patch of fairly high values (~1 V) at ~20 m at 90 km along the line (i.e., along southwestern Burger). Beam transmission was high everywhere (indicating clear water), with the lowest values (<90%) found in the lower half of the water column.

The south–south section from Cruise WWW1302 (Figure 24) differed from the west–east section in having a strong upper-layer thermohaline front centered near km 65 along the line (i.e., in the Transitional stations near northern Klondike). North of this front, mixed layer temperatures were <2 °C and salinities were <30, indicating the presence of MW, whereas waters south of the front consisted of BSW. Below the pycnocline and progressing from south to north, temperatures decreased from 2 °C to –1.5 °C and salinities increased from ~31.5 to >32.5. The coldest (<–1 °C) and saltiest (>32.5) waters of the bottom layer were located north of the surface front and beneath the pycnocline. Consequently, the pycnocline was weak along the southern end of the section but increased in strength substantially north of, and coincident with, the front. Fluorescence was weak everywhere except a zone 20–25 m deep (i.e., just below the pycnocline) 80–100 km along the line (i.e., in the Transitional stations immediately south of Statoil). Beam transmission exceeded 90% everywhere except for the bottom layer south of the front and within the patch of high fluorescence.

The final section from Cruise WWW1302 runs diagonally from the southwestern corner of Klondike to the northeastern corner of Burger (Figure 25). This section is similar to the south–north section in having a strong, shallow front (at km 125 i.e., near central Burger) separating MW to the northeast from BSW to the southwest. Also of note are the changes in the pycnocline structure: this layer is weak and temperature-dominated in the southwest, whereas it is strong and salinity-dominated in the northeast. The distribution of fluorescence and beam transmission are similar to the other sections.

The spatial coverage of sampling during Cruise WWW1304 was broader than that on the first cruise, allowing the construction of a larger number of sections. There are two west–east transects, the first across the northern boundary of Klondike and the southern boundary of Burger (Figure 26) and the second along the northern boundary of Burger and across Statoil (Figure 27). The section across Klondike and Burger indicates a 20-m-deep mixed layer having temperatures of 2 °C and salinities of 31 (i.e., BSW; Figure 26). In comparison to the August section, the pycnocline was thinner (although still very strong) and had deepened from being centered at ~15 m to 22 m depth. WW occupied the lower half of the water-column, and its properties were similar to those in August. There was no fluorescence, and the beam transmission fell below 90% only in the bottom 10–20 m, indicating the influence of the bottom boundary layer in re-suspending material. Surface layer temperatures on the section across Statoil and Burger were quite cold (–1 to +1 °C), and salinities ranged between 28 and 30—all properties indicative of MW (Figure 27). A strong 5-m-thick pycnocline separated the surface

mixed layer from the cold, salty WW in the bottom layer. Of particular interest along this section are the boluses of warmer water observed between 15 and 20 m depth. The westernmost bolus is ~10 m thick and has temperatures of between 1°C and 4°C, whereas the shallower bolus at km 40 has maximum temperatures of ~1.5 °C. The temperature and salinity characteristics of these boluses indicate that they are either intrusions or remnants of intrusions whose origin is BSW that was subducted into the pycnocline earlier (also see below).

The south–north section through Klondike and Statoil (Figure 28) is similar in coverage to the section displayed for the August cruise (Figure 24), except that ice-retreat allowed us to include additional stations to the north of those occupied in August. In many ways, the water properties along both sections are similar to one another in that a strong front occurs at km 60 and separates BSW (to the south) from MW (to the north) and that WW occupies the bottom layer. BSW within the mixed-layer was confined to the southernmost 50 km of the transect; temperatures in that layer were 2–3 °C cooler than those of August, suggesting considerable cooling over the intervening period. Below the pycnocline, WW as cold as –1 °C extended along the entire section, whereas it was confined to the northern half of the line during the August survey, suggesting that the pool of WW was moving toward the southwest. The most striking feature of this section is the appearance again of warm (>2 °C) boluses of BSW (e.g., at km 70, km 100, and km 150) within the pycnocline. These intrusions of BSW probably were subducted along the front between BSW and MW. Fluorescence again was weak except below the pycnocline between 60 and 100 km along the line (i.e., from northeastern Klondike to western Burger), and the transmissivity distribution was similar to that found on other sections.

The vertical section that runs diagonally from southwest to northeast across Klondike and Burger had property distributions very similar to those observed in August, except that the BSW found in the mixed layer had cooled by 2–3 °C since August and the front separating the BSW from the MW appeared to have weakened (Figure 29). There was no signature of the subduction process evident in the previous figure.

The final section extended northwestward from the coast (near the 10-m isobath) across Burger and Statoil and into the eastern end of the Central Channel (i.e., the DBO line; Figure 30). Within 30 km of the coast, the water-column was well-mixed, with temperatures of 2–4 °C and salinities <30. This nearshore, well-mixed water was more turbid than the offshore water, in that the beam transmittance is <90% everywhere. The increase in turbidity probably was caused by bottom resuspension that then is distributed over these shallow, unstratified waters. Farther seaward, the upper 15–20 m of the water also was well-mixed, but there were pockets of cool (<1 °C), low-salinity (<30.5) water distributed across the section. The freshest water occurred at the far end of the section and consisted of MW sitting above warmer, moderately saline BSW that probably had penetrated eastward from the Central Channel. WW occurred in the bottom layer over the middle of the line and was part of the mass of WW associated with Hanna Shoal that extends into Burger and Statoil.

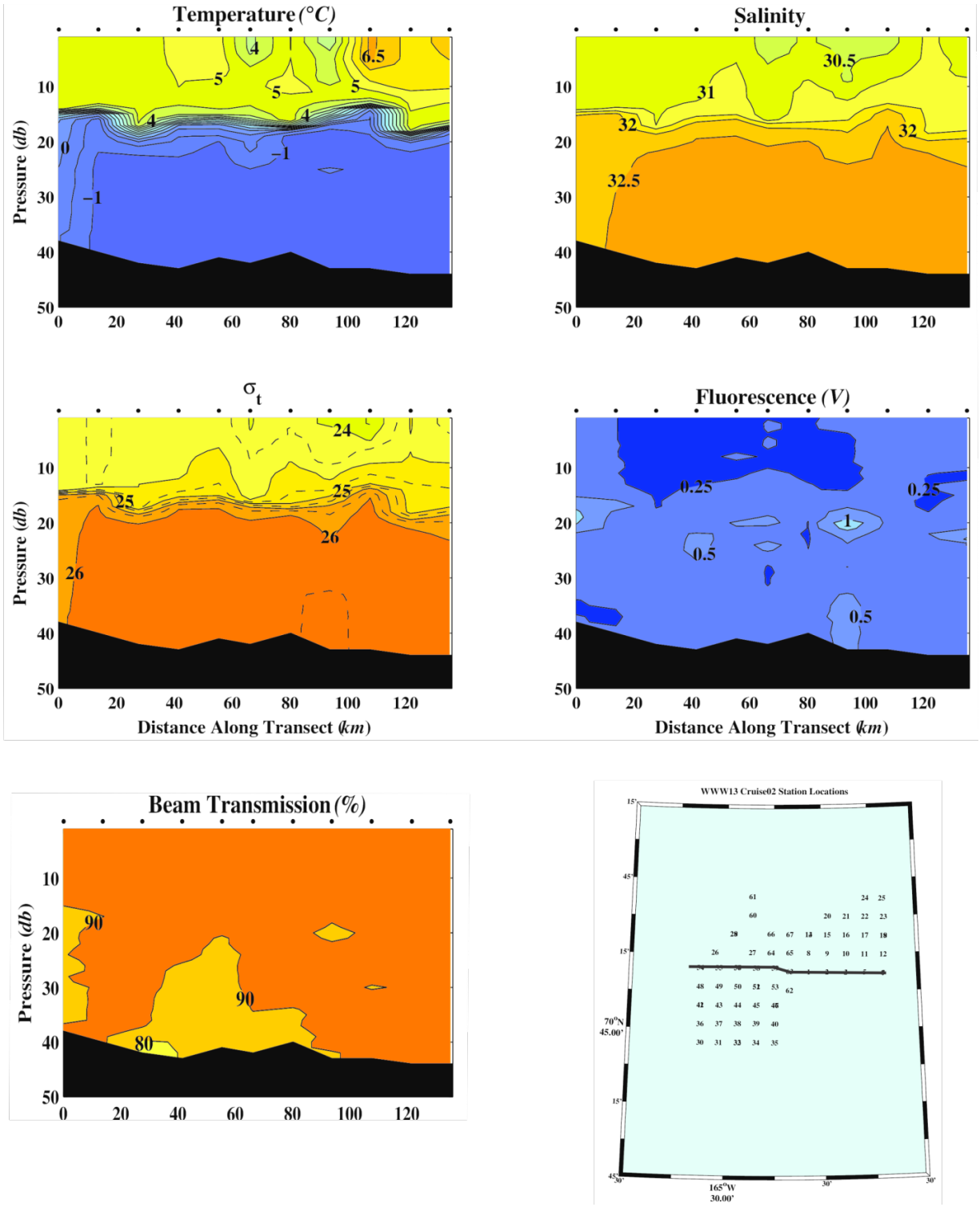

Figure 23. The west–east section across Klondike and Burger of temperature, salinity, sigma-t, fluorescence, and beam transmission from the 11–23 August 2013 survey (Cruise WWW1302). Stations in the vertical sections are aligned from west (left) to east (right).

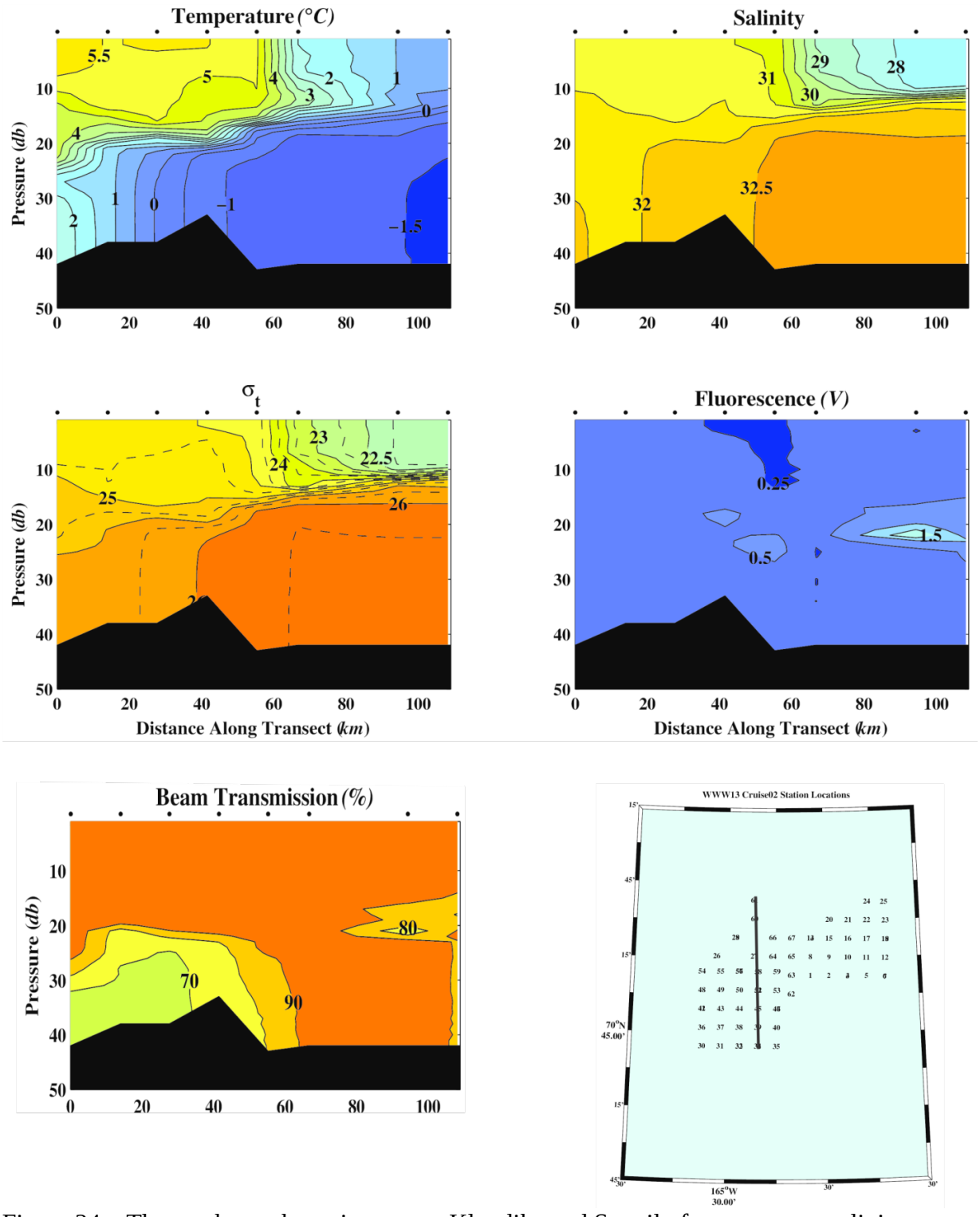

Figure 24. The south–north section across Klondike and Statoil of temperature, salinity, sigma-t, fluorescence and beam transmission from the 11 - 23 August 2013 survey (Cruise WWW1302). The stations in the sections are aligned from south (left) to north (right).

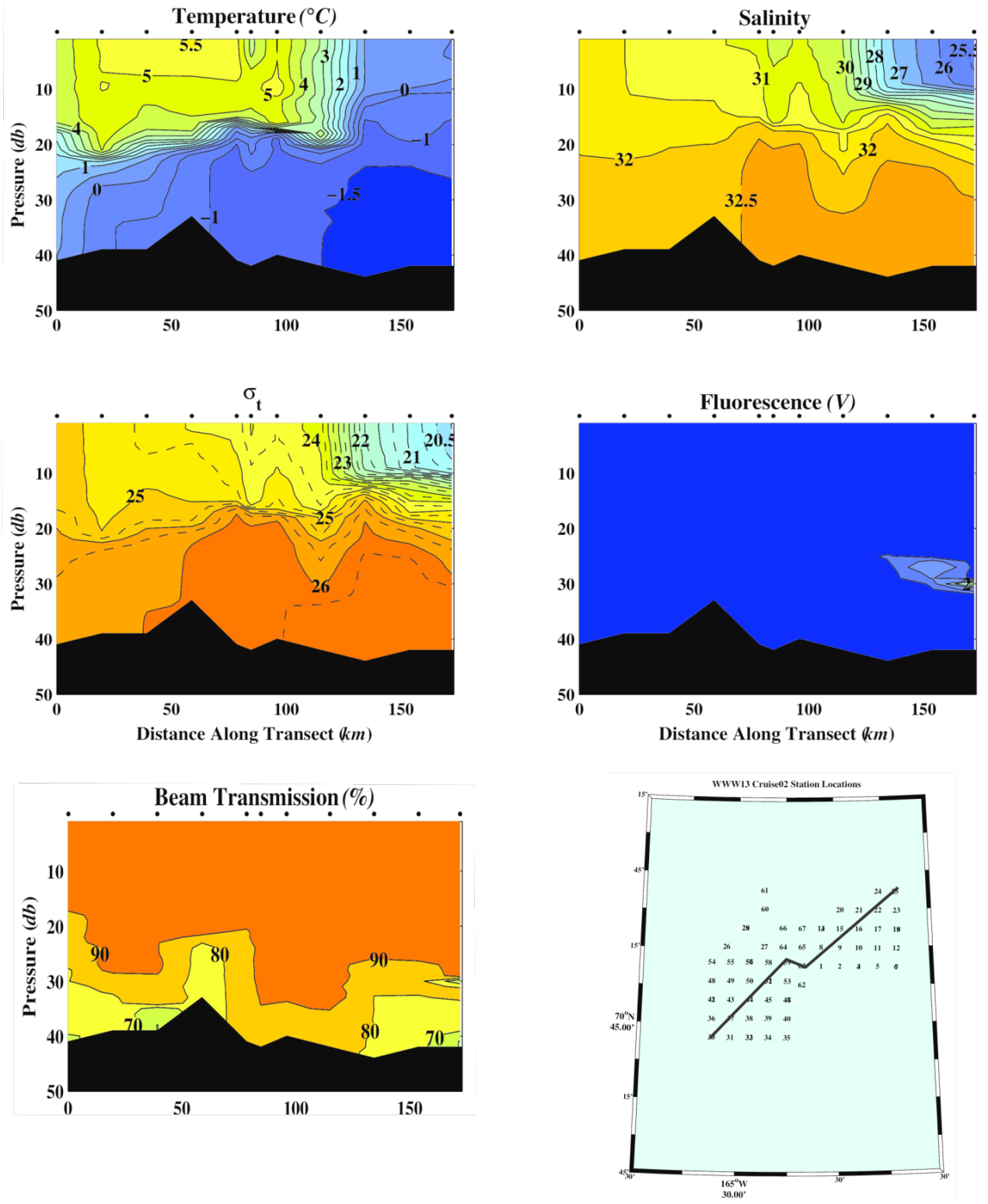

Figure 25. The southwest-northeast section across Klondike and Burger of temperature, salinity, sigma-t, fluorescence and beam transmission from the 11 - 23 August 2013 survey (Cruise WWW1302). The stations in the sections are aligned from southwest (left) to northeast (right).

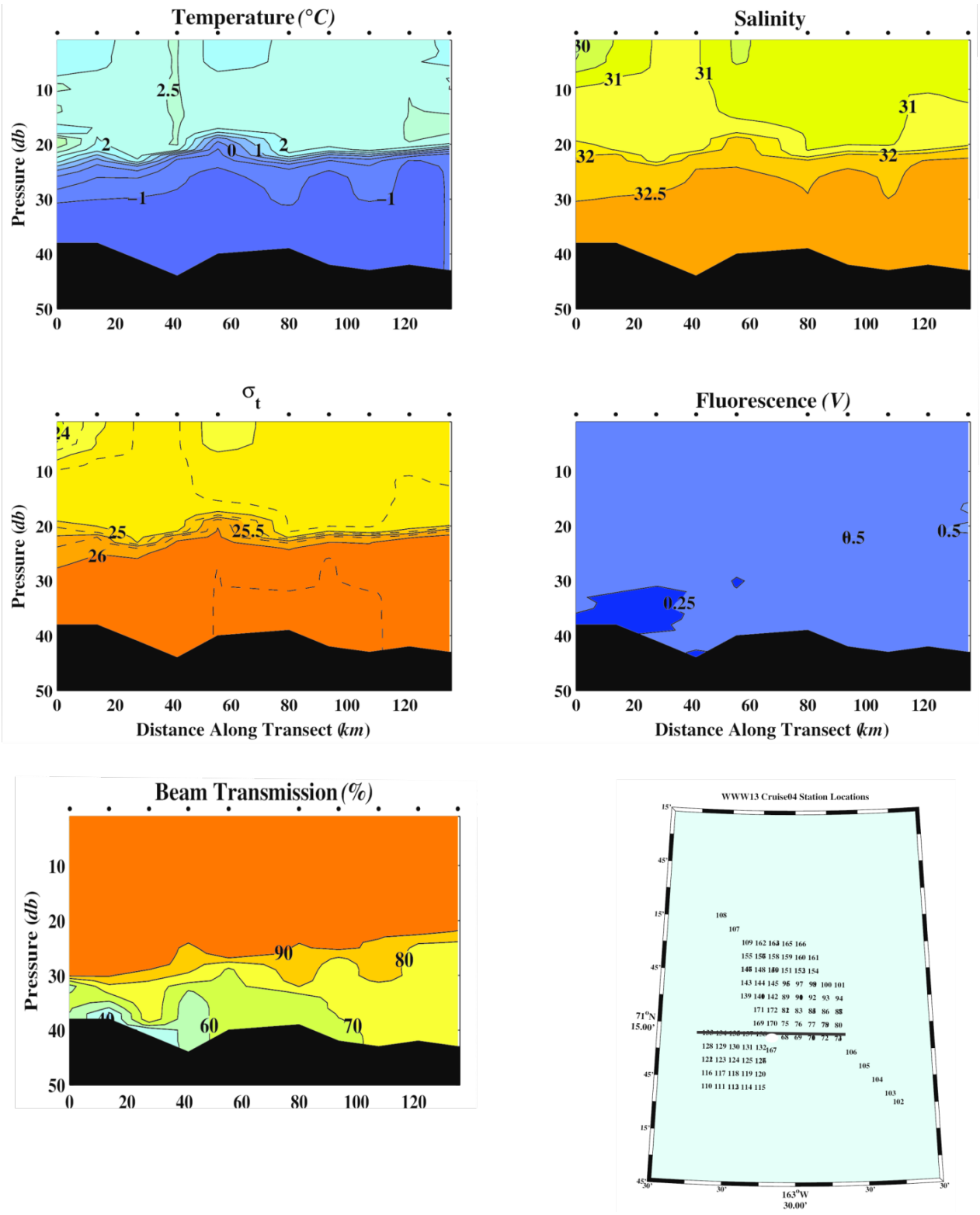

Figure 26. The west–east section across Klondike and Burger of temperature, salinity, sigma-t, fluorescence and beam transmission from the 20 September – 8 October 2013 survey (Cruise WWW1304). The stations in the sections are aligned from west (left) to east (right).

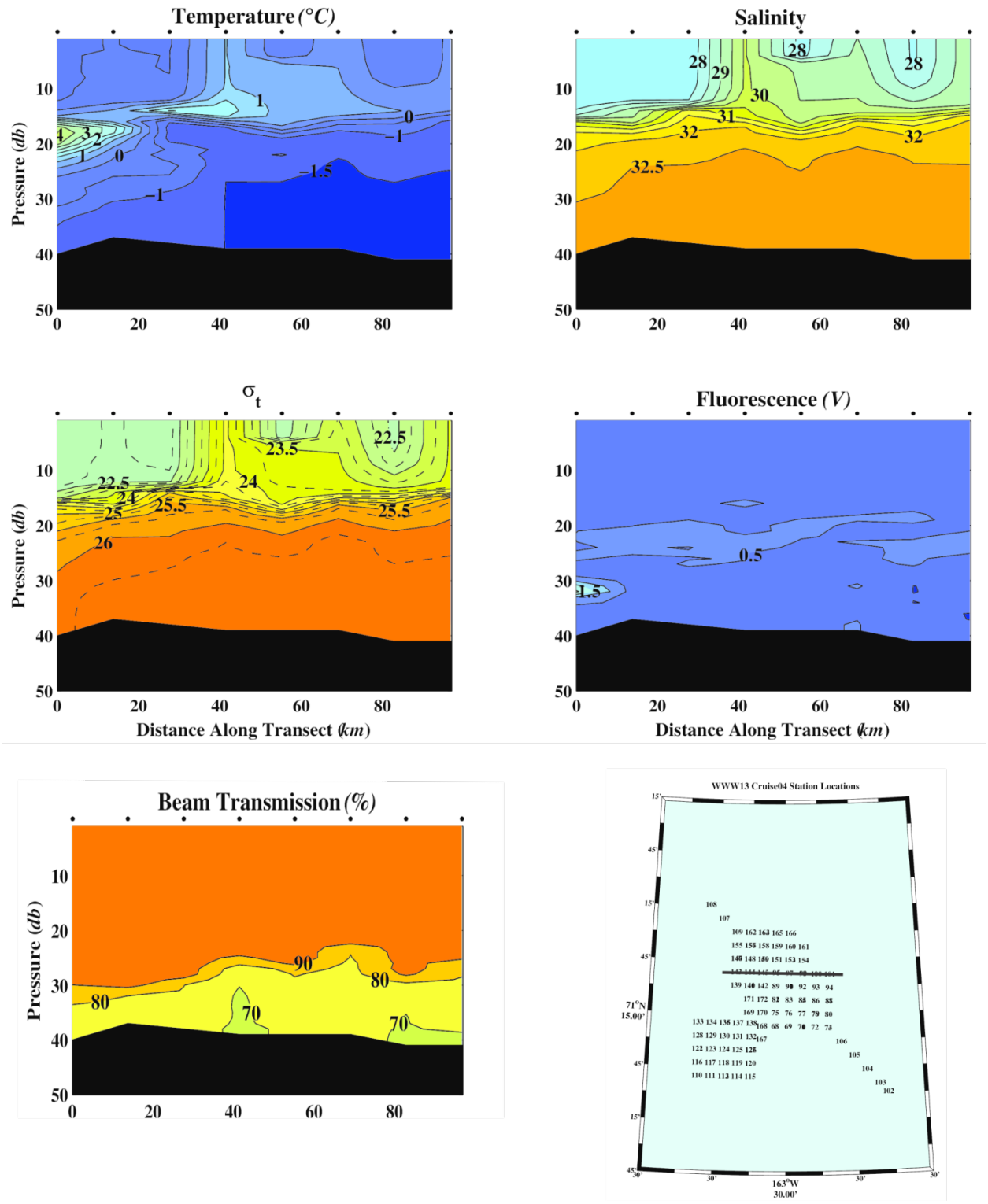

Figure 27. West–east section across Statoil and Burger of temperature, salinity, sigma-t, fluorescence and beam transmission from the 20 September – 8 October 2013 survey (Cruise WWW1302). The stations in the sections are aligned from west (left) to east (right).

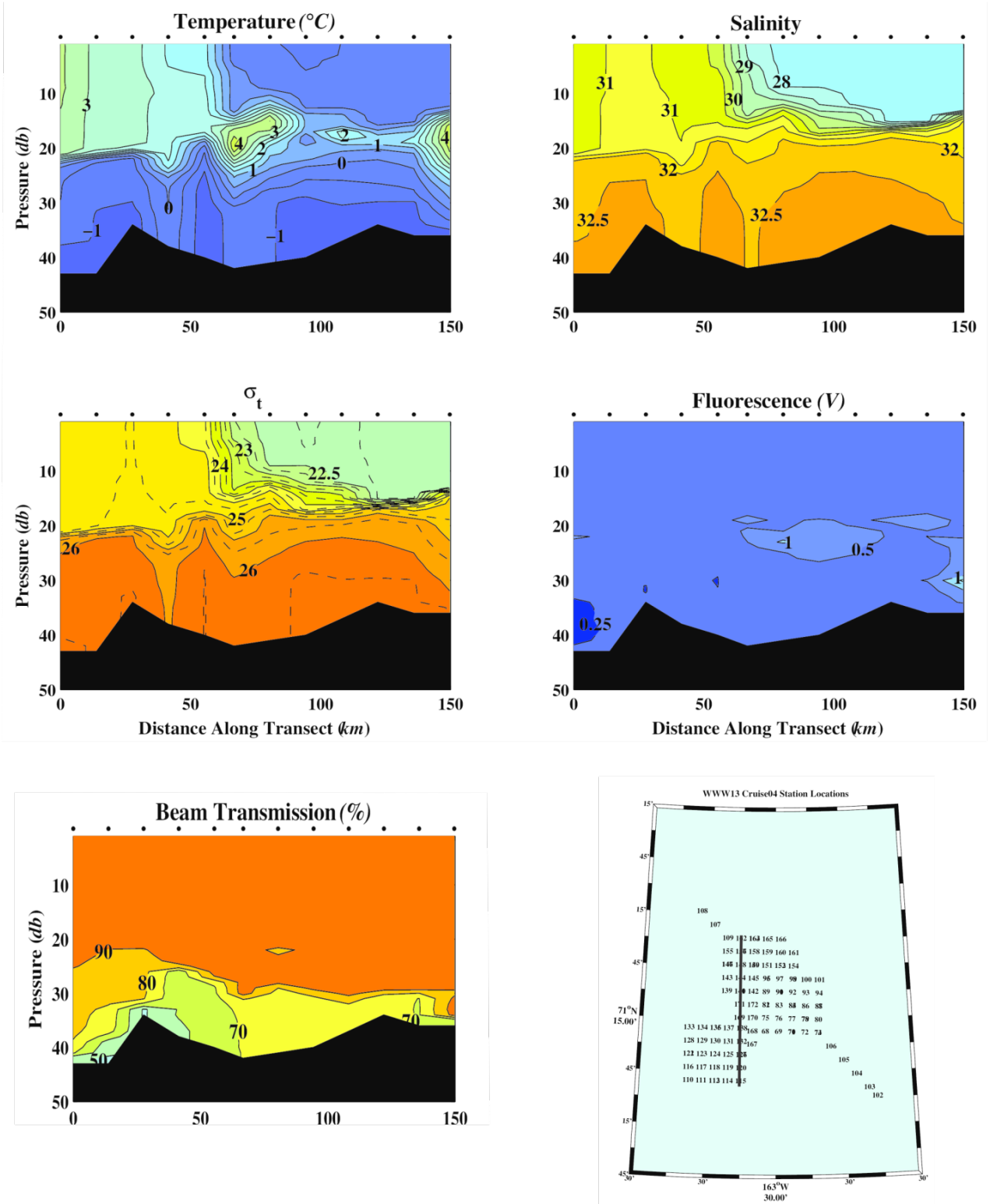

Figure 28. South–north section across Klondike and Statoil of temperature, salinity, sigma-t, fluorescence and beam transmission from the 20 September – 8 October 2013 survey (Cruise WWW1302). The stations in the sections are aligned from south (left) to north (right).

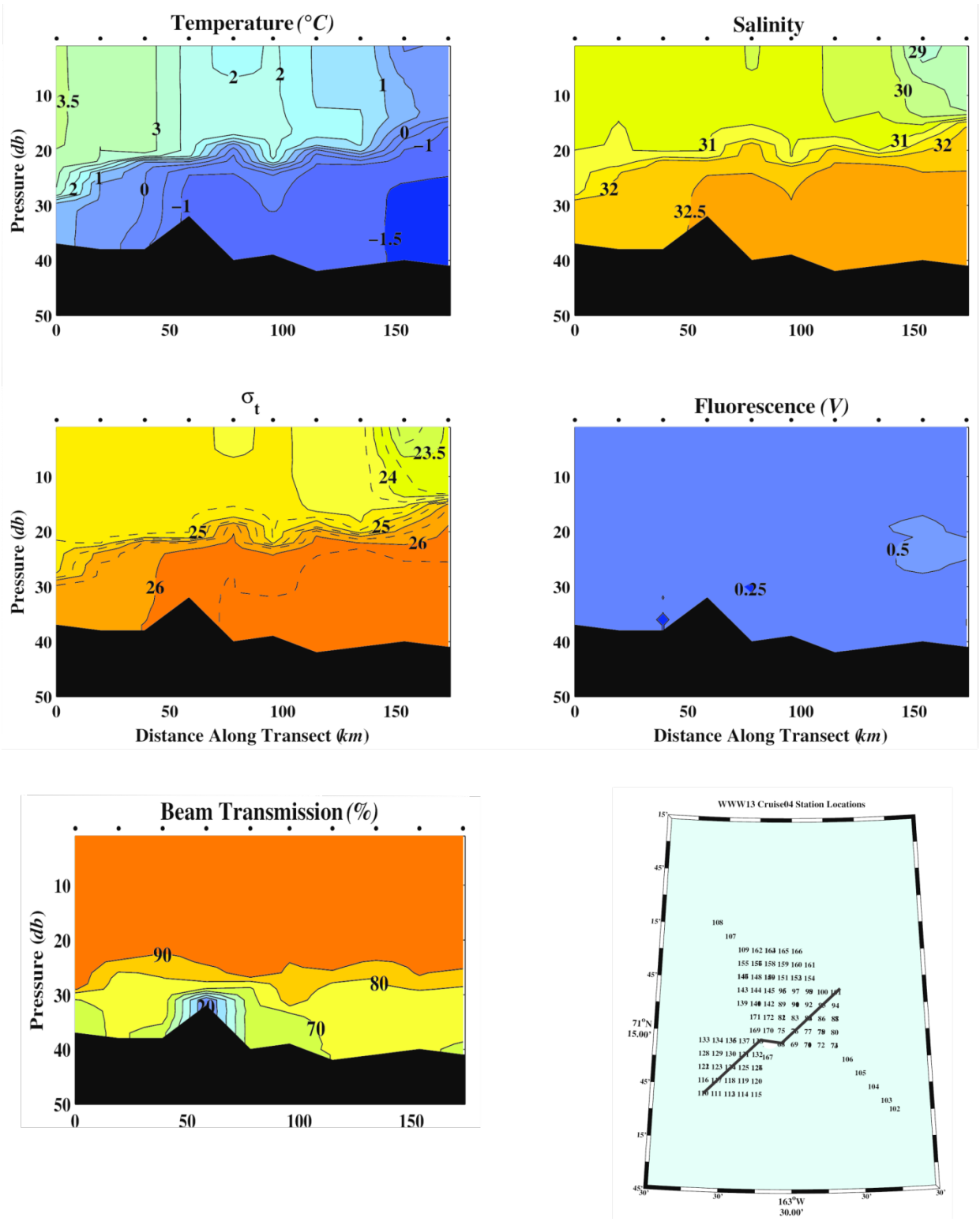

Figure 29. Southwest–northeast section across Klondike and Burger of temperature, salinity, sigma-t, fluorescence and beam transmission from the 20 September – 8 October 2013 survey (Cruise WWW1302). The stations in the sections are aligned from southwest (left) to northeast (right).

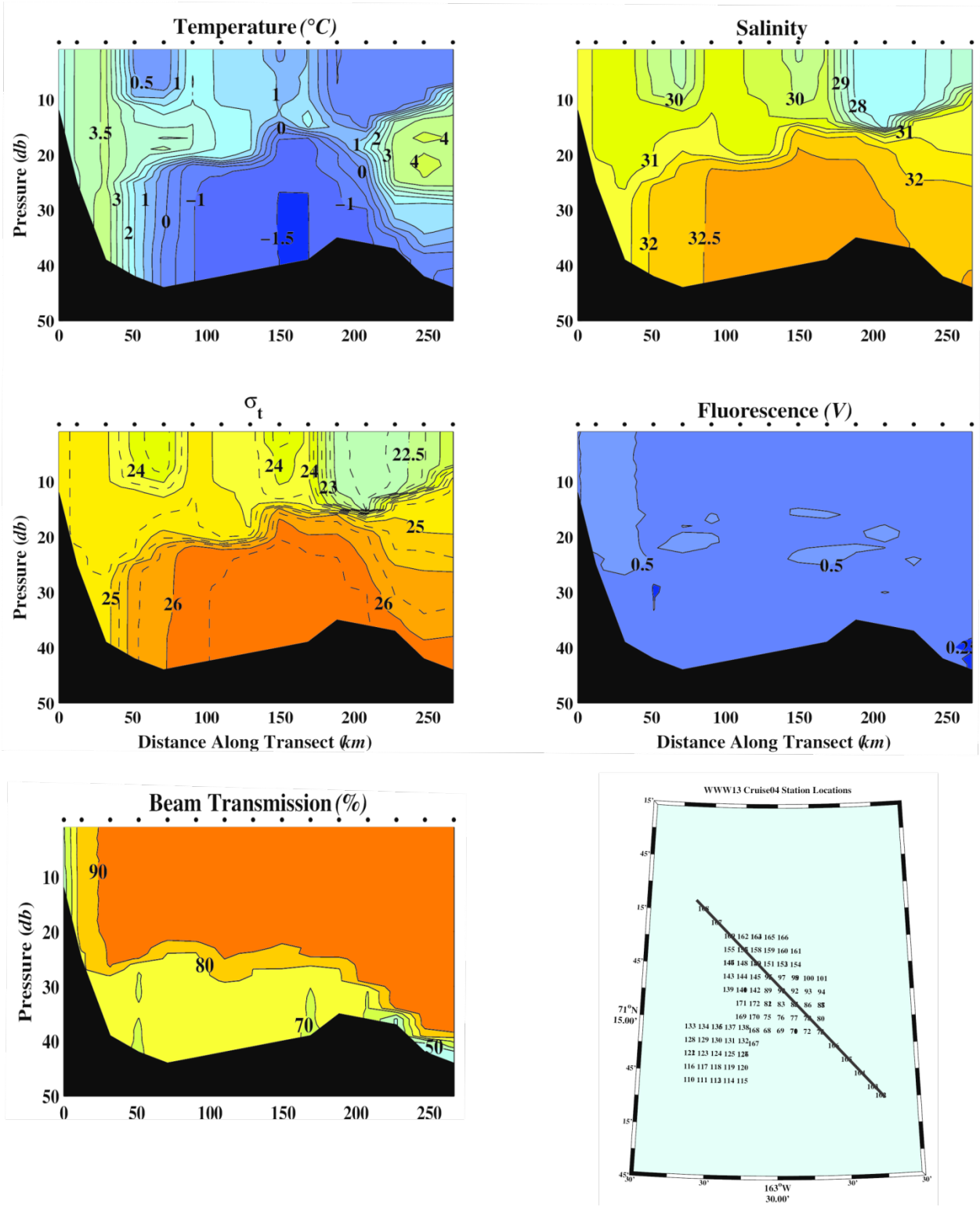

Figure 30. Southeast–northwest section from inshore and across Burger and Statoil of temperature, salinity, sigma-t, fluorescence and beam transmission from the 20 September – 8 October 2013 survey (Cruise WWW1302). The stations in the sections are aligned from southeast (left) to northwest (right).

HORIZONTAL PROPERTY DISTRIBUTIONS

We conclude this section by examining the horizontal distributions of temperature and salinity averaged over the upper 10 m and the bottom 5 m in 2013 (Figures 30 and 31). The surface maps indicate that, during the first cruise (WWW1302; August), warm, moderately saline BSW was present in Klondike and that it had not penetrated much farther northward by the second cruise (WWW1304; September). As previously noted, temperatures in the upper 10 m decreased in Klondike and within the southern half of Burger from the first to second cruise; however, there was little overall change in salinity, with two exceptions. The first exception was the salinity increase over the northern half of Burger, which may have been due to enhanced vertical or horizontal mixing that brought saltier water into the area. The other exception was the southward penetration of meltwater along the juncture of Klondike, Burger, and Statoil along ~ 164 °W.

The bottom temperature and salinity distributions indicate very little change in the gross distribution pattern of temperature and salinity between the cruises (Figure 32). This observation suggests that there has been little replacement, either by mixing or advection, of the bottom water over the 2013 season.

ADDITIONAL VERTICAL SECTIONS

The CSESP hydrographic data set suggests that the front between BSW and MW trended from west to east from mid-August to early September and moved but little over this period, in spite of the persistent northeasterly winds. Several additional sets of CTD observations, obtained under BOEM funding with a towed-CTD vehicle and provided by P. Winsor (UAF), support this hypothesis (Figures 33–39). The vehicle includes an optical sensor that measures color-dissolved organic matter (CDOM) in addition to transmissivity and fluorescence. These sections (denoted legs in the following figures) were collected in mid-September and, when viewed in conjunction with the CSESP data sets, suggest that this front persisted in strength and location throughout the 2013 field season. Such fronts were also a prominent feature of the 2012 hydrography and were detectable in the surface-current fields measured by shore-based high-frequency radars (Weingartner et al. 2013c). Radar data also were collected in 2013, although the final processing of these data was incomplete at this time. Once those data are processed, we will examine them for signatures of frontal processes. We also include a towed-CTD section that extends to the northwest from the northwestern corner of Hanna Shoal (Figure 36). Two features of note on this section are: (1) the warmest water (BSW) occurs at the northwestern end of the section and is almost certainly a portion of the flow from the Central Channel; (2) there are warm, moderately saline intrusions embedded in the pycnocline (highlighted by white ellipses in the figure). These intrusions are similar to the intrusions noted in several of the CSESP sections discussed previously.

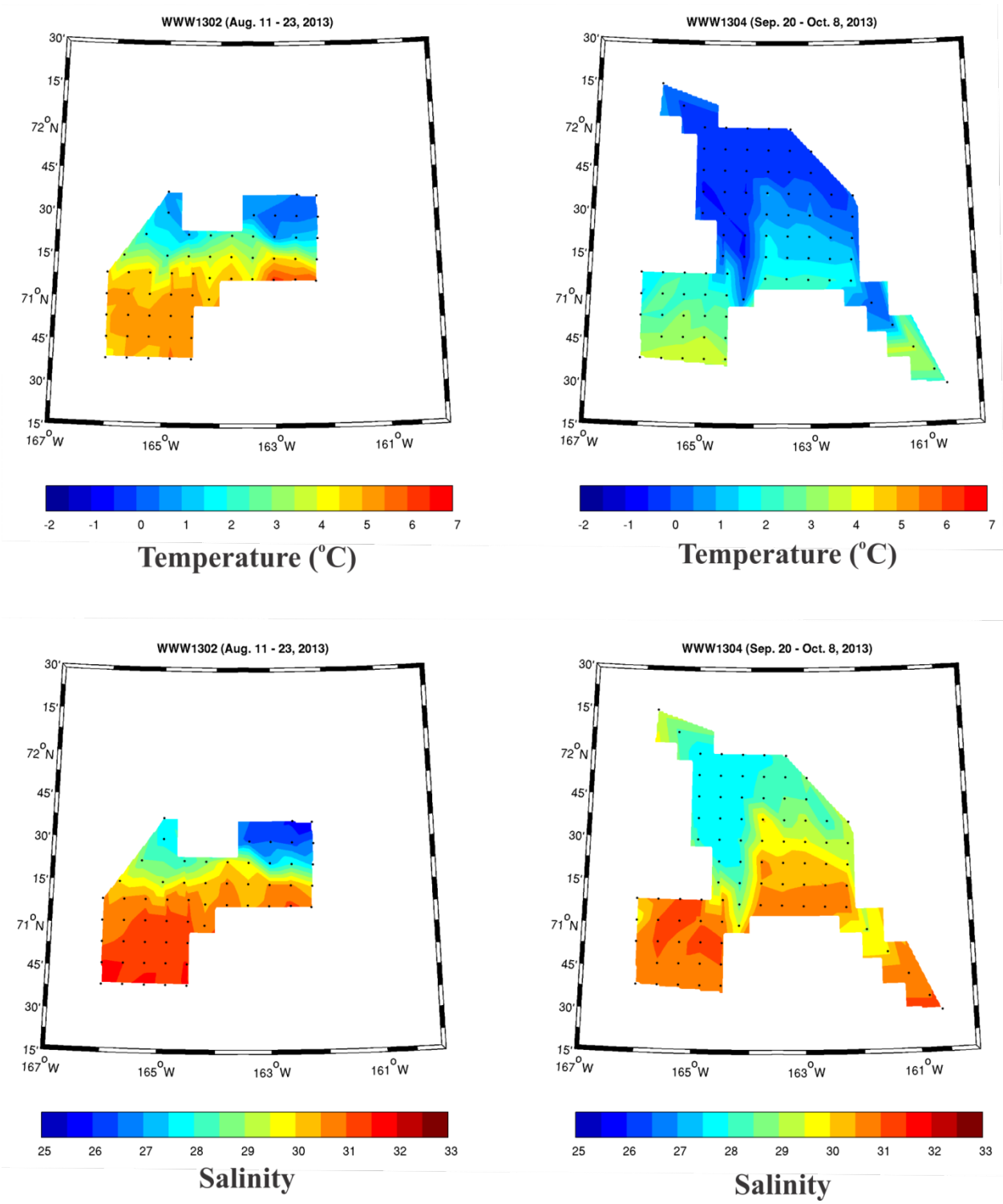

Figure 31. Average temperatures (top) and salinities (bottom) over the uppermost 10 m of the water column for the 11–23 August (left) and 20 September–8 October (right) cruises .

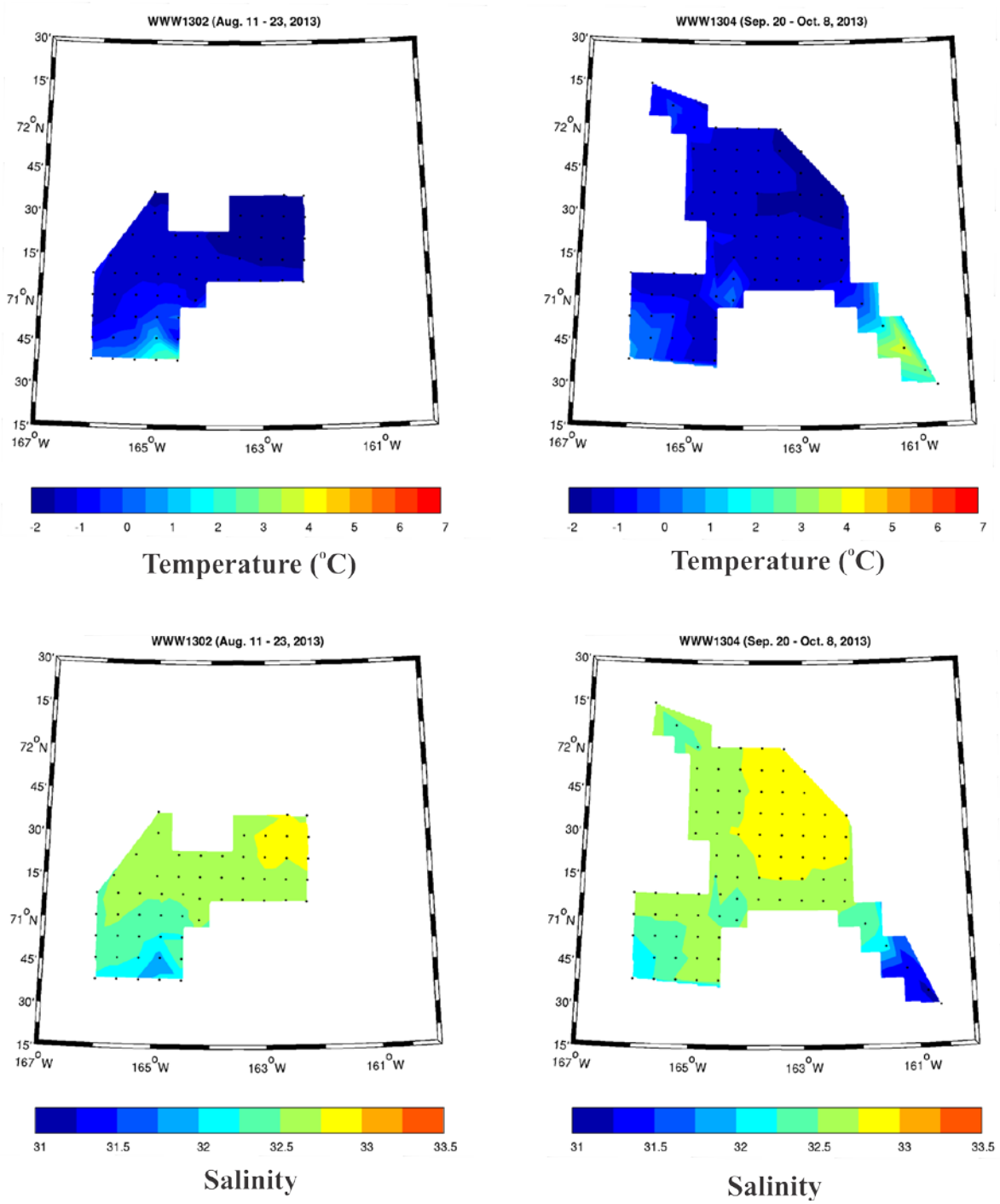

Figure 32. Average temperatures (top) and salinities (bottom) over the bottom 5m of the water column for the 11–23 August (left) and 20 September– 8October (right) cruises.

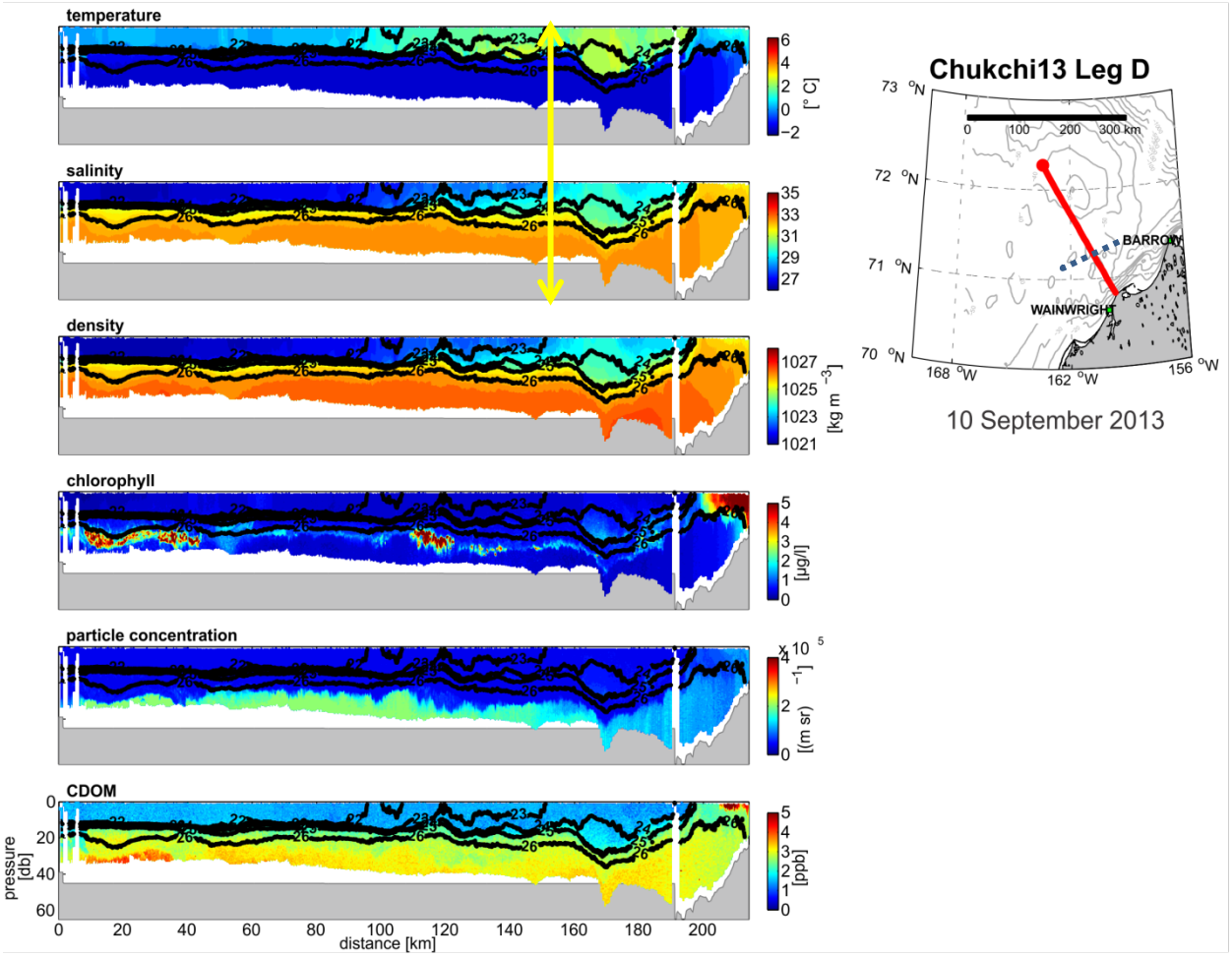

Figure 33. The Leg D vertical section derived from the towed-CTD (acrobat) on 10 September 2013. The section extends from Hanna Shoal (left side) to the coast (right side), as indicated by the inset map. From top to bottom: temperature, salinity density, chlorophyll, particle concentrations, and color dissolved organic matter (CDOM). The red dot on the map indicates the start of the section at km = 0. The dotted line on the map shows the approximate location of the front highlighted by the yellow arrow in the section. Isopycnal lines are drawn in black on each section.

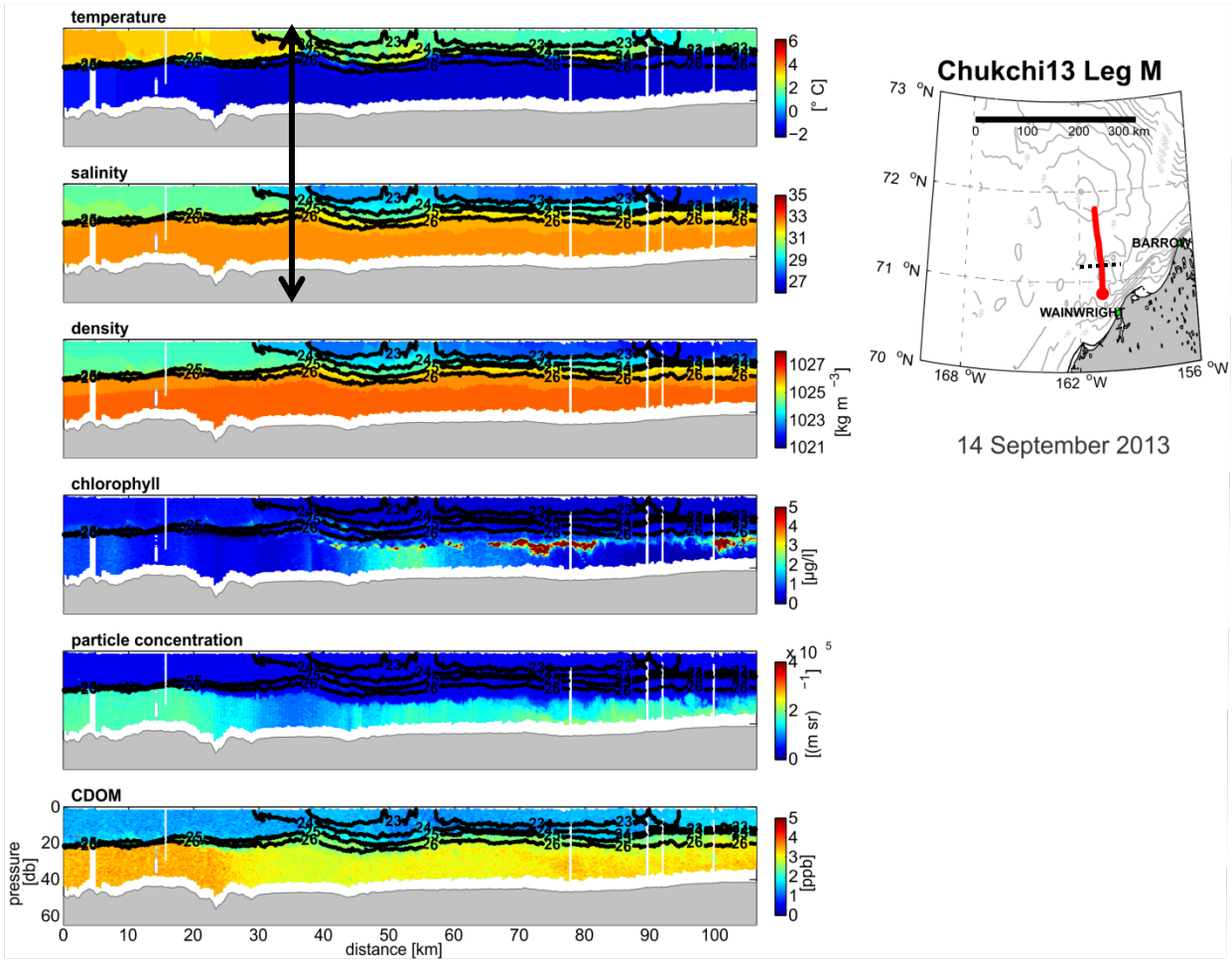

Figure 34. The Leg M vertical section derived from the towed-CTD (acrobat) on 10 September 2013. The section extends from the coast (left) to Hanna Shoal (right), as indicated by the inset map. From top to bottom: temperature, salinity density, chlorophyll, particle concentrations, and color dissolved organic matter (CDOM). The red dot on the map indicates the start of the section at km = 0. The dotted line on the map shows the approximate location of the front highlighted by the black arrow in the section. Isopycnal lines are drawn in black on each section.

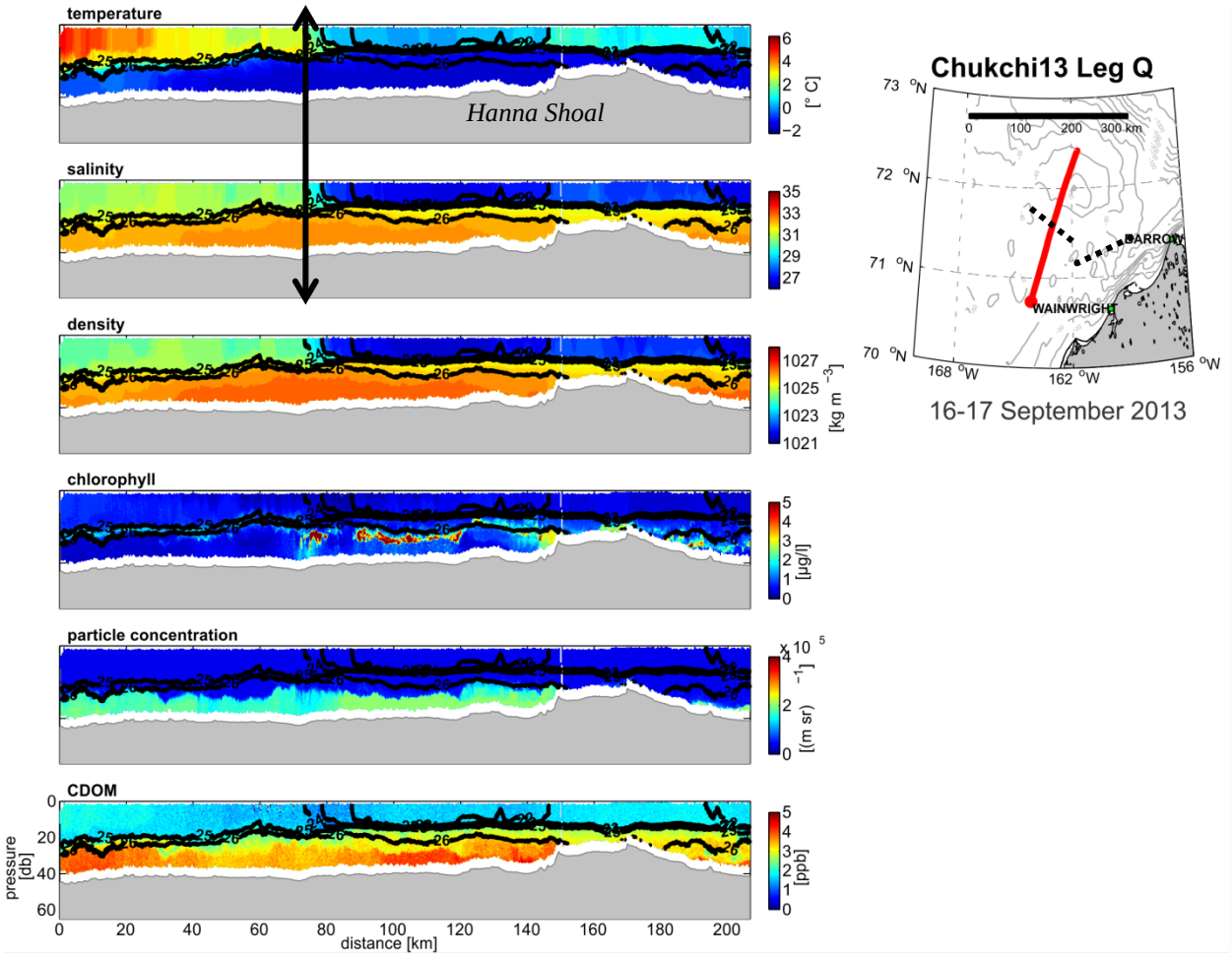

Figure 35. The Leg Q vertical section derived from the towed-CTD (acrobat) on 16–17 September 2013. The section extends northward across Hanna Shoal as indicated by the inset map. From top to bottom: temperature, salinity density, chlorophyll, particle concentrations, and color dissolved organic matter (CDOM). The red dot on the map indicates the start of the section, which is km = 0. The dotted lines on the map shows the approximate location of the front highlighted by the black arrow in this section and the estimated frontal location based on Figures 32 and 33. Isopycnal lines are drawn in black on each section.

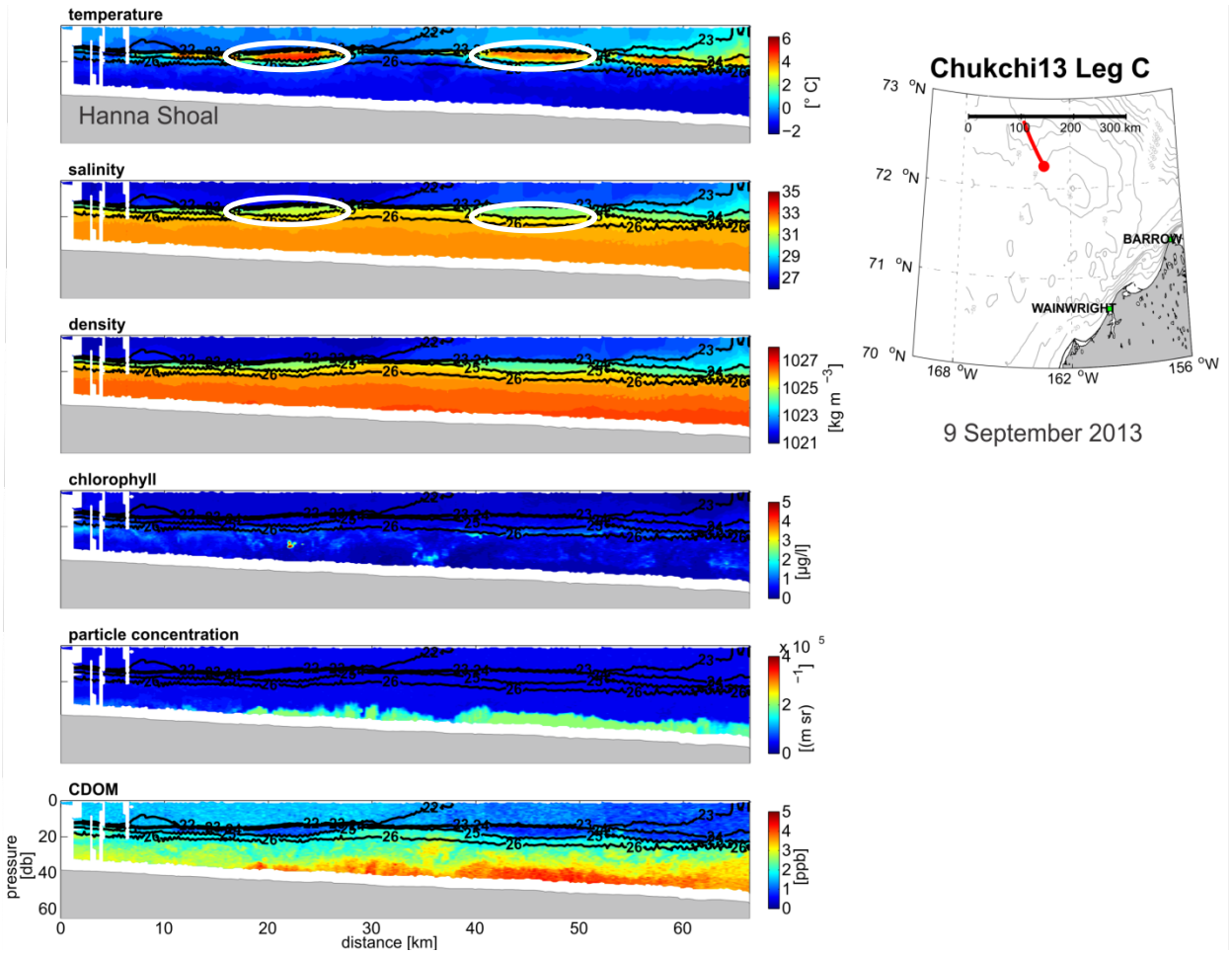

Figure 36. The Leg C vertical section derived from the towed-CTD (acrobat) on 9 September 2013. The section extends northwestward from Hanna Shoal as indicated by the inset map. From top to bottom: temperature, salinity density, chlorophyll, particle concentrations, and color dissolved organic matter (CDOM). The red dot on the map indicates the start of the section, which is km = 0. The locations outlined by white ellipses in the temperature and salinity sections indicate regions of BSW that has been subducted into the pycnocline, separating WW at depth from MW in the mixed layer. Isopycnal lines are drawn in black on each section. Isopycnal lines are drawn in black on each section.

DISCUSSION AND CONCLUSIONS

Similar to 2012, hydrographic conditions in 2013 were heavily influenced by extensive and persistent sea ice in the northeastern Chukchi Sea, especially over Hanna Shoal. The persistent ice was a regional feature that was limited primarily to the northern Chukchi shelf. As in 2012, the persistent ice cover was probably related to the grounding of large multi-year ice floes on Hanna Shoal during the preceding winter (A. Mahoney, UAF pers. comm.). Once grounded, these floes probably coalesced into a much larger ice sheet as first-year ice was advected against the grounded sheet and subsequently deformed. Attachment and deformation would increase the volume and area of the ice on Hanna Shoal. In addition, the persistent and strong northeasterly

winds of August 2013 also almost certainly played a role in maintaining ice over the Shoal into September. These winds certainly retarded and possibly halted the northward flow of warmer BSW into the northeast Chukchi Sea, and particularly into the study region: it appears that BSW was present in the Central Channel based on the limited hydrography and on the Pt. Lay drifter cluster and the Wainwright drifters. Indeed, the persistence of near-freezing, salty subsurface WW in the lower half of the water-column throughout the entire study area indicates that BSW basically was unable to penetrate the region at depth during the open-water season in 2013. In previous years, the WW generally was confined to the more northern portions of the study area in September.

The MW, which had salinities of 27–30, generally was confined to the upper 15 m of the water-column and overlaid very dense WW having salinities ≥32.5. The vertical distribution of these water masses resulted in a strongly stratified water-column that persisted into the fall. This stratification contrasts with many of the previous years, in which stratification weakened in the fall as more of the moderately stratified BSW was advected over the shelf and gradually displaced the highly stratified MW/WW structure. This replacement of the stratified water with the BSW was severely limited in 2013, appearing to have occurred only in the southernmost part of Klondike. The large volume of MW was accompanied by an extensive and prominent frontal system at the surface between it and the BSW. This front was approximately zonally-oriented and extended from Statoil eastward to Barrow Canyon. Unlike 2012, when this front appeared to migrate northward through September, the front's location was stationary or near-stationary during the entire period.

Several of the hydrographic sections from both 2012 and 2103 suggest that BSW, which has a density intermediate between that of MW and that of WW, subducts along the meltwater front and then penetrate laterally into the pycnocline (Figure 37). Two other sections illustrating similar features from P. Winsor's towed-CTD sections also are shown (Figures 38 and 39).

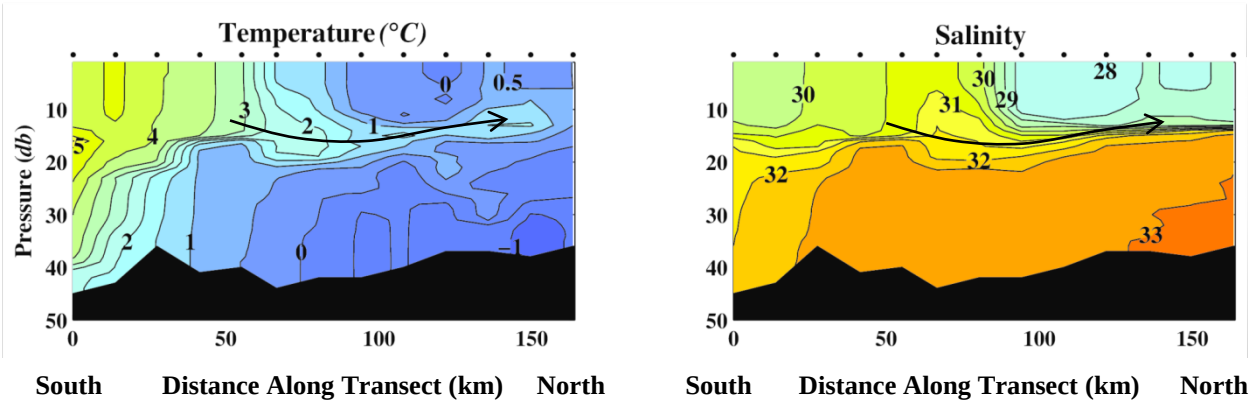

Figure 37. A south–north transect across Klondike, Statoil and the southern flank of Hanna Shoal in 2012 (from Weingartner et al., 2013), with arrows suggesting the intrusion of BSW into the pycnocline separating MW (on the top) and WW (on the bottom). (From Weingartner et al., 2012).

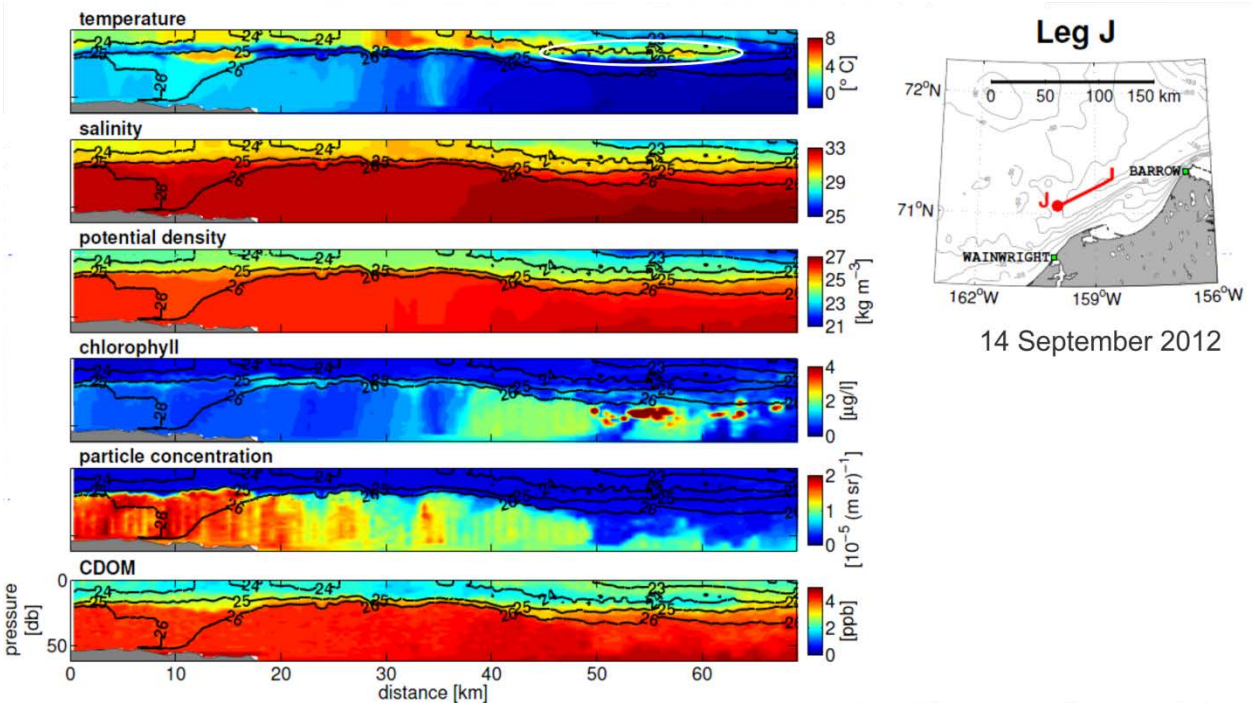

Figure 38. The Leg J vertical section derived from the towed-CTD (acrobat) on 14 September 2012. The section extends southeastward along the western side of Barrow Canyon, as indicated by the inset map. From top to bottom: temperature, salinity density, chlorophyll, particle concentrations, and color dissolved organic matter (CDOM). The red dot on the map indicates the start of the section, which is km = 0. The white ellipse on the temperature section shows a subducting tongue of BSW beneath the MW at the front between the two water-masses.

In aggregate, the sections from 2012 and 2013 suggest that such subductive features are common and that all are linked to processes occurring along the front between the MW and the BSW. These observations raise the question of how warm BSW affects ice-melt and ice-retreat. Although we cannot address this issue with the data on hand, the BSW is denser than the MW, so it may not directly contribute to lateral melting of the sea-ice along the periphery of the ice-edge. Instead, subducted flows of warm BSW may be the mechanism by which heat first is transferred laterally beneath the ice (and MW layer) and then is diffused upward to melt the underside of the ice. Such a mechanism suggests that ice melt arises through a complicated advective–diffusive balance whose attributes are dictated by the strength and position of the front, the pycnocline, and the properties of the BSW in a particular year.

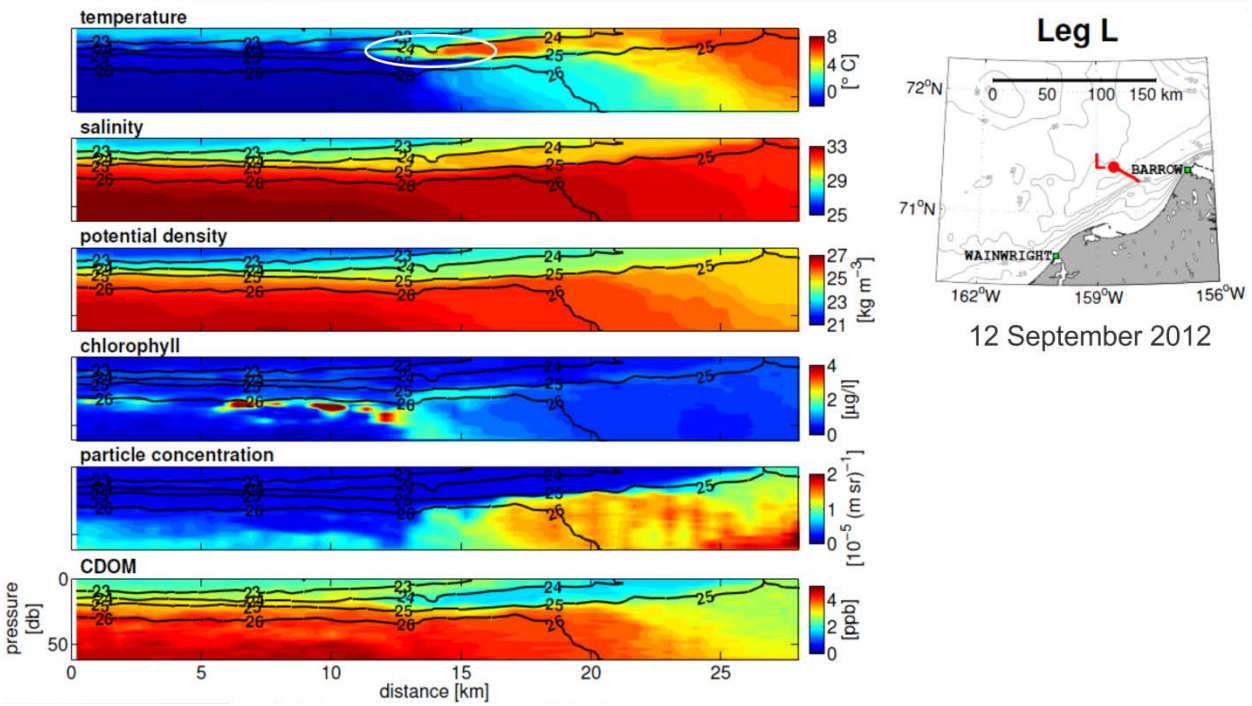

Figure 39. The Leg L vertical section derived from the towed-CTD (acrobat) on 14 September 2012. The section extends southeastward along the western side of Barrow Canyon, as indicated by the inset map. From top to bottom: temperature, salinity density, chlorophyll, particle concentrations, and color dissolved organic matter (CDOM). The red dot on the map indicates the start of the section, which is km = 0. The white ellipse on the temperature section shows a subducting tongue of BSW beneath the MW at the front between the two water-masses.

The model described in the Methods section was run for 30 days. Although we have examined the results for each day, we show results from Day 1 and Day 30 only for purposes of brevity and because these results capture the salient points (Figures 40 and 41). The frontal structure is baroclinically unstable, which leads to the rapid development of unstable frontal waves (Day 1) and eddy formation (within days). Frontal instability severely distorts the front and causes a cross-frontal exchange of salt and meltwater. In particular, mixtures of BSW and MW form northward-propagating cyclonic (counter-clockwise) eddies with diameters of 5–20 km and azimuthal velocities of 5–20 cm s^{-1}. In Model 1, frontal deformation is caused by cyclonic and anti-cyclonic vortex pairs (see Day 30). In contrast, well defined cyclonic eddies consisting of meltwater have detached from the front and slender, energetic filaments of ~50 km in length permeate the frontal zone in Model 2.

Vertical sections of temperature across the middle of the channel for the same days show intrusions of warm water into the pycnocline separating the meltwater and the winter water (Figure 41). (Although not shown, the salinity sections show very similar structures.) The intrusions appear blob-like in the model, but they are associated with the eddies and filaments seen in Figure 40. Several features are apparent. The intrusions vary in thickness from 5 m to 25 m and in width from a few km to ~10 km. In both model runs, the intrusions appear as a train of blobs, rather than as a continuous plume, in contrast to the observations (e.g., Figure 37).

However, the low horizontal resolution of the sampling upon which Figure 37 is based may result in discrete features that are smeared by the contouring routine used in constructing the section. On the other hand, the simplifications incorporated upon which the model runs are based (discussed next) may inhibit the formation of plumes. Nevertheless, we tentatively suggest that the model results are in broad agreement with the observations. Our results suggest that the intrusions arise as a consequence of baroclinic instability of the front between BSW and MW. Moreover, both frontal structures are unstable, suggesting that subducted intrusions will form, regardless of the stratification properties of the BSW. However, it appears that the eddies are more energetic in Model 2 than in Model 1. Although a more thorough analysis is required to quantify the differences between models, they may be because the available potential energy and geostrophic velocity shear of Model 2 exceeds that of Model 1. Because baroclinic instabilities convert available potential energy into eddy energy, the eddy energy should be proportional to the initial available potential energy.

We caution that these model runs are only a preliminary investigation into the cause for the subducting plumes. Consequently, there are several limitations associated with the models. For example, we have ignored wind forcing so that vertical diffusion effectively will be absent. Moreover, we purposely have ignored the effects of bottom friction at this stage of the investigation but point out that this absence is not realistic because the shelf is so shallow. Bottom friction will bleed energy from the eddies and may dampen their formation; at the very least, these eddies will increase the developmental time of the instabilities. Other issues that may affect the outcome are that our initial conditions effectively represent a step-function changes in the vertical and horizontal stratification. In contrast, the observed stratification and frontal widths are finite. Finally, our channel width is only 150 km, so, by Day 30, the eddy characteristics may be influenced as these features approach the channel walls. Additional modeling exercises are underway to assess the effects of these limitations; these additional exercises will be reported on in the future. Our ultimate goal with respect to modeling is to estimate the cross-frontal heat flux and to determine whether the vertical heat flux associated with these intrusions influences the rate of ice-melt. To determine whether this heat flux actually is important in affecting the rate of melt, we eventually will incorporate ice into the model and examine its response to differences in wind-forcing, water properties, and hydrographic structures. Conceptually, vertical diffusion of heat from the subducting tongues may be a mechanism for enhancing ice melt. There also is the potential for a negative feedback between ice-melt and the vertical diffusion of oceanic heat. This feedback arises because summer solar heating will result in meltwater being added to the surface layer beneath the ice sheet. This positive buoyancy flux enhances upper-ocean stratification and will inhibit vertical diffusion.

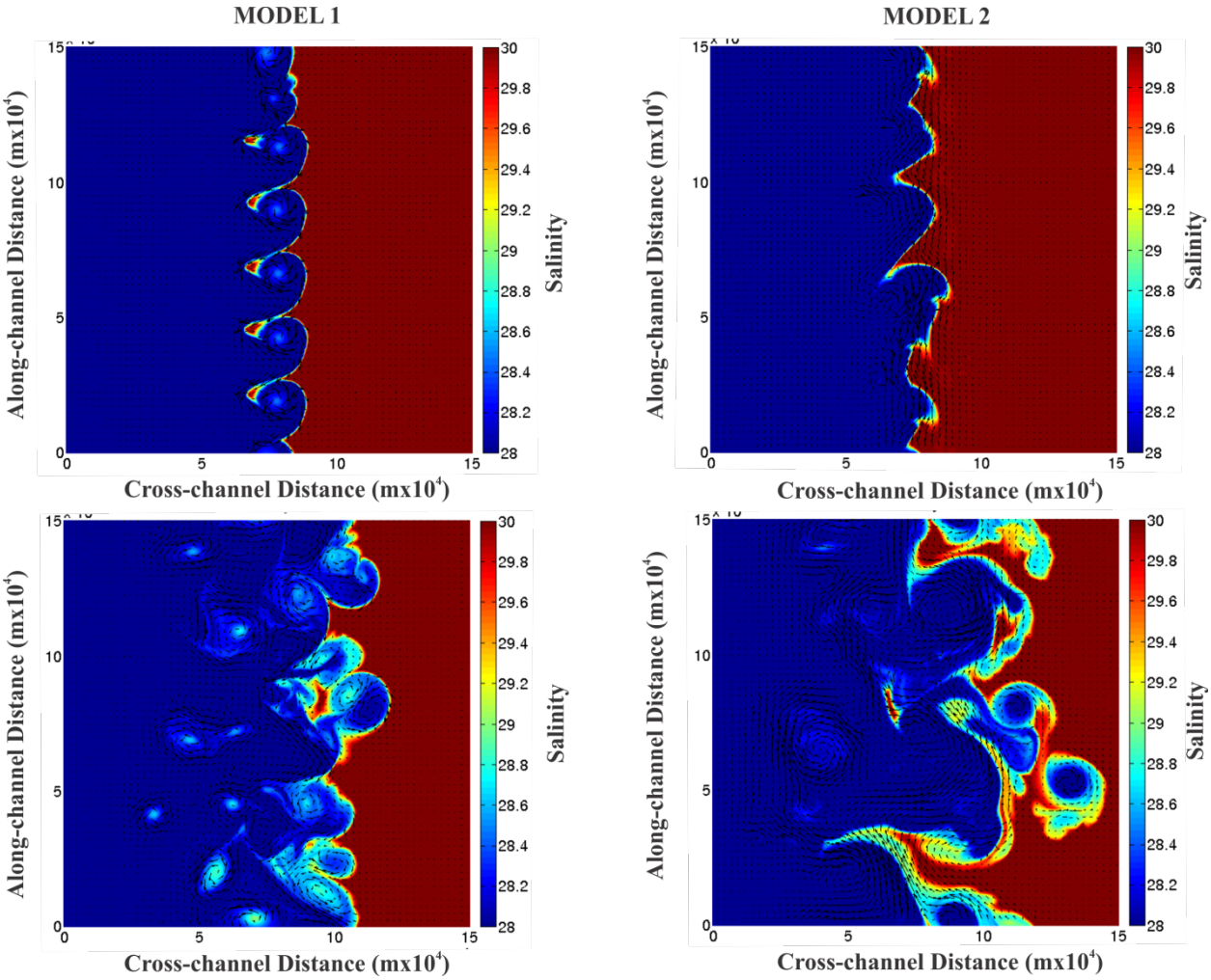

Figure 40. Plan views of the surface-salinity and -velocity fields from Model 1 (left) and Model 2 (right) on Day 1 (top) and Day 30 (bottom). The maximal velocity vector is ~0.2 m s^{-1}.

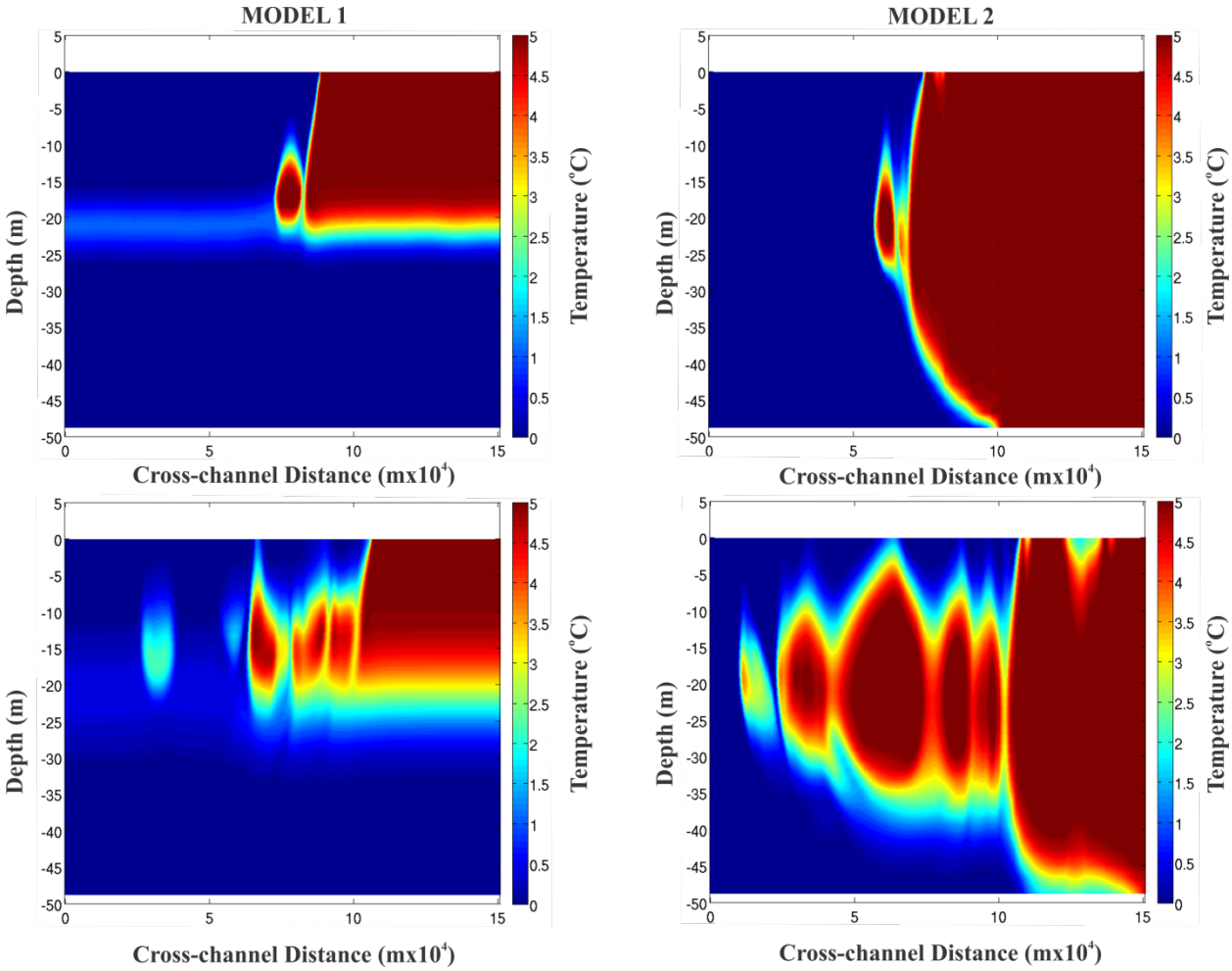

Figure 41. Vertical sections of temperature across the middle of the channel from Model 1 (left) and Model 2 (right) on Day 1 (top) and Day 30 (bottom).

Finally we note that there may be a connection between the principal component results and the simple model. We noted that August PC1 mode was correlated, to some degree, with the zonal wind stress. Westward winds led to reduced ice concentrations and eastward winds led to increased ice concentrations. Westward winds tend to enhance downwelling at the ice-edge, which will steepen the isopycnals at the MW/BSW front (e.g., Model 2), and, by increasing available potential energy and the geostrophic velocity shear, enhance instability. If the instabilities result in a substantial heat flux to the underside of the ice, subsurface melting may be promoted. These same winds promote a northward Ekman drift of the sea-ice. Although this motion should enhance ice retreat, it moves the ice into colder water and possibly increases ice concentrations. In contrast, eastward winds promote upwelling along the ice-edge and a southward Ekman drift. In this case, the instabilities may be weaker than for the downwelling wind case (because the isopycnals at the front are horizontally inclined and the geostrophic shear is smaller), so the cross-frontal eddy heat flux is diminished. However, Ekman dynamics will cause the ice to drift into warmer water and, thus, increase melt rates and reduce ice concentrations. Our finding that wind-speed anomalies are correlated with diminished ice cover suggests that stormier conditions promote breakup and ice-melt by exposing a greater surface

area to the sun and/or warm water. Enhanced vertical mixing induced by the winds may increase the diffusion of heat into the ice from subsurface waters. How these competing tendencies affect the net rate of ice melt and ice retreat have yet to be explored, but the simple model presented here is a first step in resolving these issues.

Because the correlation between zonal winds and ice concentration indicates only a modest influence of the zonal winds on ice concentration, other factors certainly must be at play. These other factors include variability in the atmospheric radiation and the oceanic reservoir of heat. The former is measureable from meteorological buoys, but these are difficult to maintain in ice. Alternatively, this variable is available from re-analysis fields produced by meteorological models, but their accuracy is problematic at high latitudes (Walsh et al., 2009). The oceanic reservoir of heat flux is controlled by processes that affect the heat flux through Bering Strait and its eventual transport across the Chukchi Sea shelf. Although a quantification of the variability in the heat flux through Bering Strait is being developed (Woodgate et al., 2012), the available time-series is too short to assess statistically its importance in summer ice-retreat. If we find that subducting plumes play a role in ice melt, the model results presented here indicate that the efficacy of this flux is a function of the stratification of the BSW moving northward into the Chukchi Sea. Understanding the evolution of this stratification and its interannual variability also may be critical in understanding oceanic heat fluxes into the pack ice.

ACKNOWLEDGMENTS

We thank the officers and crews of the *Westward Wind* for their skill and efficiency in conducting the at-sea work. P. Winsor (UAF) kindly provided the acrobat CTD sections shown herein. L. DeSousa, B. Adams, R. Suydam (Barrow), and W. Neatok (Pt. Lay) conducted the 2013 drifter deployments under the sponsorship of the North Slope Borough–Shell Baseline Studies Program. The 2011 and 2012 drifter deployments were sponsored by the Coastal Marine Institute with co-funding from Shell. Ms. KoFan Lu conducted the model runs with assistance from K. Hedstrom. S. Wisdom worked wonders in executing complicated field programs. Scientific discussions with R. Day, A. Blanchard, and R. Hopcroft enhanced T. Weingartner's understanding of the Chukchi Sea. Finally we thank the ConocoPhillips, Shell Exploration & Production Company, and Statoil USA Exploration & Production, Inc. for their support throughout all phases of the CSESP.

REFERENCES

Coachman, L. K., Aagaard, K., and Tripp, R.B., 1975. Bering Strait: The Regional Physical Oceanography. University of Washington Press, Seattle, WA. 172 pp.

Danielson, S., T. Weingartner, K. Hedstrom, K. Aagaard, R. Woodgate, E. Curchitser, and P. Stabeno. in press. Ekman transport, continental shelf waves, and variations of the Pacific–Arctic sea-surface-height gradient: coupled wind-forced controls of the Bering–Chukchi shelf circulation and the Bering Strait throughflow. Progress in Oceanography.

Mesinger, F., and 19 Coauthors, 2006. North American regional re-analysis. Bulletin of the American Meteorological Society 87, 343–360.

North G. R., T. L. Bell, R. F. Cahalan, and F. J. Moeng, 1982: Sampling errors in the estimation of empirical orthogonal functions. Monthly Weather Review, 110, 699–706.

Pickart, R.S., Weingartner, T., Pratt, L.J., Zimmermann, S., and Torres, D.J., 2005. Flow of winter-transformed Pacific water into the western Arctic. Deep-Sea Research (Part II 52), 3175–3198.

Shroyer, E. L., and Plueddemann, A.J., in press. Wind-driven modification of the Alaskan coastal current. Journal of Geophysical Research.

Spall, M. A., 2007. Circulation and water mass transformation in a model of the Chukchi Sea. Journal of Geophysical Research 112, C05025. doi:10.1029/2005JC002264

Spreen, G., Kaleschke, L., and Heygster, G., 2008. Sea ice remote sensing using AMSR-E 89 GHz channels. Journal of Geophysical Research 113, C02S03. <doi:10.1029/2005JC003384>

Walsh, J.E, Chapman, W.L., and Portis, D., 2009. Arctic cloud fraction and radiative fluxes in atmospheric reanalyses. Journal of Climate 22, 2316–2334.

Walsh, J.J., McRoy, C.P., Coachman, L.K., Goering, J.J., Nihoul, J.J., Whitledge, T.E., Blackburn, T. H., Parker, P.L., Wirick, C.D., Shuert, P.G., Grebmeier, J.M., Springer, A.M., Tripp, R.D., Hansell, D.A., Djenedi, S., Deleersnijder, S., Henriksen, K., Lund, B.A., Andersen, P., Müller-Karger, F.E., and Dean, K., 1989. Carbon and nitrogen cycling within the Bering/Chukchi seas: source regions for organic matter affecting AOU demands of the Arctic Ocean. Progress in Oceanography 22, 277–359.

Weingartner, T., C. Irvine, C., Dobbins, E., Danielson, S., DeSousa, L., Adams, B., Suydam, R., and Neatok, W., 2014. Satellite-tracked drifter measurements in the Chukchi and Beaufort seas. Final Report, University of Alaska Coastal Marine Institute. 241 p.

Weingartner, T., Dobbins, E., Danielson, S., Winsor, P., Potter, R., and Statscewich, H., 2013a. Hydrographic variability over the northeastern Chukchi Sea shelf in summer-fall 2008–2010. Continental Shelf Research 67, 5–22. <http://dx.doi.org/10.1016/j.csr.2013.03.012>

Weingartner, T., Winsor, P., Potter, R., Statscewich, H., and Dobbins, E., 2013b. Application of high frequency radar to potential hydrocarbon development areas in the northeast Chukchi Sea. Report to U.S. Bureau of Ocean Energy Management, Alaska Outer Continental Shelf Region, ConocoPhillips, Inc., and Shell Exploration & Production Company, Anchorage, AK, by Institute of Marine Sciences, University of Alaska, Fairbanks, AK. 162 pp.

Weingartner, T., Aagaard, K., Woodgate, R., Danielson, S., Sasaki, Y., and Cavalieri, D., 2005. Circulation on the north central Chukchi Sea Shelf. Deep-Sea Research *(*Part II), 52, 3150–3174. <doi:10.1016/j.dsr2.2005.10.015>

Winsor, P., and Chapman, D.C., 2004. Pathways of Pacific water across the Chukchi Sea: a numerical model study. Journal of Geophysical Research 109, C03002, doi: 1029/2003JC001962

Woodgate, R.A., Aagaard, K., and Weingartner, T.J., 2005a. Monthly temperature, salinity, and transport variability of the Bering Strait through flow. Geophysical Research Letters 32, L04601. <doi:10.1029/2004GL021880>

Woodgate, R.A., Aagaard, K., and Weingartner, T.J., 2005b. A year in the physical oceanography of the Chukchi Sea: moored measurements from autumn 1990–1991, Deep-Sea Research (Part II), 52 (24–26), 3116–3149.

Woodgate, R.A., Weingartner, T., and Lindsay, R., 2012. Observed increases in oceanic fluxes from the Pacific to the Arctic from 2001 to 2011 and their impacts on the Arctic. Geophysical Research Letters, 39, L24603. doi:10.1029/2012GL054092.